Title: Comprehensive analysis of A-type lamin tail region for repairing the nuclear lamina

Yohei Kono [1, 2, 3], Chan-Gi Pack [4, 5], Takehiko Ichikawa [2], Arata Komatsubara [6], Stephen A. Adam [7], Loïc Rolas [8], Sussan Nourshargh [8], Ohad Medalia [9], Robert D. Goldman [7], Takeshi Fukuma [2], Hiroshi Kimura [1, 6], Takeshi Shimi [1, 2*]

Running Head: Lamin A tail region controls the localization to the rupture sites

Author Affiliation:

[1] Cell Biology Center, Institute of Innovative Research, Tokyo Institute of Technology, Yokohama, Japan.

[2] WPI Nano Life Science Institute (WPI-NanoLSI), Kanazawa University, Kanazawa, Japan.

[3] Faculty of Frontier Engineering, Institute of Science and Engineering, Kanazawa University, Kanazawa, Japan.

[4] Convergence Medicine Research Center, Asan Institute for Life Science, Asan Medical Center, Seoul, Korea.

[5] Department of Biomedical Engineering, University of Ulsan College of Medicine, Seoul, Korea.

[6] School of Life Science and Technology, Tokyo Institute of Technology, Yokohama, Japan.

[7] Department of Cell and Developmental Biology, Feinberg School of Medicine, Northwestern University, Chicago, IL.

[8] Centre for Microvascular Research, William Harvey Research Institute, Faculty of

Medicine and Dentistry, Queen Mary University of London, London, UK.

[9] Department of Biochemistry, University of Zurich, Zurich, Switzerland.

The corresponding author:

Takeshi Shimi, Ph.D., WPI Nano Life Science Institute (WPI-NanoLSI), Kanazawa University, Kakuma-machi, Kanazawa, 920-1192, Japan.

Phone: +81-76-234-4540; E-mail: t-shimi@staff.kanazawa-u.ac.jp

Abstract

The nuclear lamina (NL) lines the inner nuclear membrane (INM) of the nuclear envelope (NE) to maintain nuclear structure in metazoan cells. The major NL components, the nuclear lamins contribute to the protection against NE rupture induced by mechanical stress. Lamin C (LC) but not lamin A (LA) is rapidly diffused from the nucleoplasm to sites of NE rupture induced by laser microirradiation in immortalized mouse embryonic fibroblasts (MEFs). However, the molecular mechanism for differentiating LA from LC with respect to the localization/accumulation at the rupture sites still remains unknown. In this study, we reveal by immunofluorescence, live-cell imaging and fluorescence correlation spectroscopy (FCS) that the CaaX motif, the second cleavage site and the LA-characteristic segment (LACS) regulate the localization of LA to the rupture sites. Our data suggest that Hutchinson–Gilford Progeria syndrome (HGPS) might exhibit the delay in localizing LA to the rupture sites through this mechanism.

Introduction

In eukaryotic cell nuclei, the nuclear envelope (NE) spatially separates the nuclear genome from the cytoplasm. The barrier function of the NE is due to two phospholipid bilayers of the inner and outer nuclear membranes (INM, ONM). The INM is in contact with chromatin at the nuclear side via INM proteins (Zullo *et al.*, 2012), whereas the ONM is connected with the cytoskeletal system through the linker of nucleoskeleton and cytoskeleton (LINC) complex (Crisp *et al.*, 2006), and is continuous with membranous organelles including the endoplasmic reticulum (ER) (Voeltz *et al.*, 2002). The nuclear lamina (NL) is closely apposed to the INM and associates with heterochromatin to support nuclear structure. Nuclear pore complexes (NPCs) fill holes formed by the INM-ONM fusion for nucleo-cytoplasmic transport and interact with euchromatin (Paine *et al.*, 1975).

The NL structure consists of the nuclear lamins and associated proteins (Foisner and Gerace, 1993). The lamins are type V intermediate filament proteins, which are subdivided into A-type lamins (lamins A [LA] and C [LC]) and B-type lamins (lamins B1 [LB1] and B2 [LB2]) (Gerace *et al.*, 1978; Gerace and Blobel, 1980). LA and LC are derived from the single gene *LMNA* by alternative splicing (Lin and Worman, 1993), whereas LB1 and LB2 are encoded by separate genes *LMNB1* and *LMNB2*, respectively (Höger *et al.*, 1990; Biamonti *et al.*, 1992; Lin and Worman, 1995; Maeno *et al.*, 1995). Lamin molecules assemble into a filament with a diameter of ~3.5 nm and these filaments appear to non-randomly lay on top of each other to form meshworks of the NL with a thickness of ~13.5 nm in immortalized mouse embryonic fibroblasts (MEFs) (Shimi *et al.*, 2015; Turgay *et al.*, 2017). LA/C and LB1 filaments associate with the outer ring structure of the NPC and are involved in regulating the distribution of the meshworks and NPCs (Shimi *et al.*, 2008; Shimi *et al.*, 2015; Turgay *et al.*, 2017; Kittisopikul *et al.*, 2021).

The −CaaX box at the C terminus of LA, LB1 and LB2 is post-translationally processed in steps, including the attachment of farnesyl group to the cysteine residue of the −CaaX box by a farnesyltransferase (Lutz *et al.*, 1992; Sinensky *et al.*, 1994), proteolytic cleavage of three residues (−aaX) by an aaX endopeptidase (Boyartchuk *et al.*, 1997) and carboxyl methylation of the terminal carboxylic acid group (−COOH) of the C-terminal cysteine residue by a carboxyl methyltransferase (Winter-Vann and Casey, 2005). The maturation of LB1 and LB2 is completed by these steps. In case of the farnesylated and carboxymethylated pre-LA, an additional 15 C-terminal residues including the farnesylated and carboxymethylated cysteine, are cleaved off by ZmpSte24/FACE1 to produce mature LA (Leung *et al.*, 2001; Corrigan *et al.*, 2005).

The NE is locally ruptured during physiological and pathological circumstances. Immediately after NE rupture, NE components are recruited to the rupture sites with the endosomal sorting complex required for transport-III (ESCRT-III) complex and Barrier-to-autointegration factor (BAF) (Denais *et al.*, 2016; Raab *et al.*, 2016; Halfmann *et al.*, 2019). Nuclear DNA adjacent to the rupture sites is recognized by the DNA sensors cyclic GMP-AMP synthase (cGAS) and its downstream signaling effector STING (Denais *et al.*, 2016; Raab *et al.*, 2016; Halfmann *et al.*, 2019). The frequency of spontaneous and forced NE rupture is significantly increased by the depletion of lamins (Vargas *et al.*, 2012; Robijns *et al.*, 2016; Chen *et al.*, 2018; Chen *et al.*, 2019). Numerous mutations have been found throughout the *LMNA* gene that cause a spectrum of human genetic disorders, collectively called laminopathies. Laminopathies associated with dilated cardiomyopathy (DCM), muscular dystrophy (MD), familial partial lipodystrophy (FPLD) and Hutchinson–Gilford Progeria syndrome (HGPS) are frequently accompanied by spontaneous NE rupture (De Vos *et al.*, 2011; Earle *et al.*, 2020; Kim *et al.*, 2021). In

HGPS, the heterozygous transversion of a nucleotide substitution at position 1824 T>C (G608G) leads to abnormal splicing of the last 150 nucleotides of exon 11, resulting in the expression of progerin (PG) which lacks 50 amino acids (residues 607–656) from the C terminus of pre-LA (Fig. 1 A). Because these residues contain the second proteolytic cleavage site involved in pre-LA processing, PG remains farnesylated and carboxymethylated, leading to its permanent association with the INM (De Sandre-Giovannoli *et al.*, 2003; Eriksson *et al.*, 2003).

Recently, we found that LC but not LA was rapidly recruited from the nucleoplasm to sites of NE rupture induced by laser microirradiation along with BAF in immortalized MEFs (Kono *et al.*, 2022). However, the molecular mechanism by which LA and LC differ in localization/accumulation kinetics at the rupture sites still remains to be elucidated. Here, we investigate the involvement of LA processing in regulating lamin localization within a relatively long-time window by immunofluorescence using MEFs with wild type (WT) and HGPS backgrounds. Our previous study by live-cell imaging demonstrated that the rapid accumulation of mEmerald-fused LA was observed only when it was overexpressed at a high level (Kono *et al.*, 2022), and the accumulation kinetics appeared to be artifactual because it was not confirmed by immunofluorescence (Kono *et al.*, 2022). Therefore, we established the ectopic expression system for live-cell imaging and fluorescence correlation spectroscopy (FCS) in which mEmerald-LA, alternate forms of LA, and mEmerald-LC are maintained at a low level by expression from the endogenous promotor in WT, HGPS and LA/C-knockout (KO) MEFs. Our data reveal the significance of the CaaX motif, the second proteolytic cleavage site and the LA-characteristic sequence (LACS) in the C-terminal tail region for regulating the localization of LA at the rupture sites. We provide further insights into the molecular

mechanism that differentiate LA from LC for lamin localization/accumulation kinetics at the rupture sites.

Results

Localization of PG and LA to the rupture sites is delayed by PG expression

To investigate the significance of the CaaX motif and the second cleavage site of pre-LA for regulating the localization kinetics at the rupture sites, we used immortalized WT MEFs and heterozygous knock-in MEFs with PG expression from a mutant allele of the *Lmna* gene carrying the c.1827C>T; p.Gly609Gly mutation (*Lmna*$^{G609G/+}$, G609G/+). This mutation is equivalent to the HGPS mutation in the human *LMNA* gene (Lopez-Mejia *et al.*, 2011; Osorio *et al.*, 2011). These cells stably expressed super-folder Cherry harboring two NLSs derived from SV40 large T antigen and c-Myc (NLS-sfCherry) as a NE rupture marker (Kono *et al.*, 2022). Because spontaneous NE rupture is frequently observed in skin fibroblasts derived from a HGPS patient (De Vos *et al.*, 2011), we first examined if G609G/+ MEFs also exhibit misshapen nuclei, the leakage of NLS-sfCherry to the cytoplasm, mislocalization of LB1 and cGAS accumulation, which are indicative of spontaneous NE rupture. WT and G609G/+ cells were stained with Hoechst 33342 for DNA and specific antibodies directed against LB1 and cGAS (Fig. S1 A). Unlike the HGPS patient cells, G609G/+ cells did not show these phenotypes compared to WT cells (Table S1), indicating that the HGPS mutation is not accompanied by spontaneous NE rupture in these MEFs. Next, to examine the effect of this mutation on recovery from forced NE rupture, single-cell compression by AFM indentation was applied to these cells, and the nuclear reentry of NLS-sfCherry was observed by time-lapse imaging before and after the induction of the rupture (Fig. 1 B) (Ivanovska *et al.*, 2023). Interestingly, G609G/+ cells showed a significantly slow reentry compared to the WT cells which had a ~50% recovery from the original fluorescence intensity ~4 min after the rupture (Fig. 1 C and D), indicating that PG expression slows the recovery from forced NE rupture.

To determine the localization kinetics of LA and PG at the rupture sites in WT and G609G/+ nuclei, these cells were fixed at 30, 60 and 120 min after the induction of NE rupture by 405-nm laser microirradiation (Fig. 1 E) (Kono *et al.*, 2022), and then stained with Hoechst 33342 for DNA and specific antibodies directed against LA and PG, which do not cross-react to each other (Fig. 1 A). LA was detected at the rupture sites in ~54.5%, ~76.7% and ~85.7% of WT nuclei, and in ~28.6%, ~61.3% and ~67.6% of G609G/+ nuclei within 30-40, 60-70 and 120-130 min after laser microirradiation, respectively (Fig. 1 F and G, Fig. S1 B), strongly suggesting that PG expression slows the localization kinetics of LA. Similarly, PG localization to the rupture sites was determined in G609G/+ cells by immunofluorescence. PG was present at the rupture sites in ~7.1%, ~32.3% and ~50.0% of G609G/+ nuclei (Fig. 1 G), indicating that the PG is significantly slower in localizing to the rupture sites than LA in WT and G609G/+ cells.

LC accumulation to the rupture sites is delayed by PG expression

The slow localization of LA and PG to the rupture sites is unlikely to be directly linked to the delay in retrieving NLS-sfCherry from the cytoplasm immediately after the induction of NE rupture (Fig. 1 C, D, F and G). Because LC rapidly accumulates at the rupture sites and the depletion slows the nuclear reentry of NLS-sfCherry at the early time points (within 10 min) (Kono *et al.*, 2022), PG expression could slow LC accumulation. To test this idea, endogenous LA, LC and PG were directly labeled with a LA/C-specific genetically encoded probe, designed ankyrin repeat protein (DARPin)-LaA_6 (Zwerger *et al.*, 2015), fused with super-folder GFP (sfGFP), sfGFP-DARPin-LA6 in WT and G609G/+ MEFs expressing NLS-sfCherry (Kono *et al.*, 2022) (Fig. 2 A). Because endogenous LA and PG did not localize to the rupture sites within 180 s after the induction

of NE rupture (Kono *et al.*, 2022) (Fig. 1 B and C, Fig. S1 B), sfGFP-DARPin-LA6 accumulating at the rupture sites only represented endogenous LC within the short-time window. After laser microirradiation, the accumulation of sfGFP-DARPin-LA6 at the rupture sites was significantly slower in G609G/+ cells compared to WT cells (Fig. 2 B and C), indicating that PG expression reduced LC accumulation.

Because nucleoplasmic LC diffuses to the rupture sites (Kono *et al.*, 2022), the diffusion fraction could be decreased in G609G/+ cells compared to WT cells. To test this idea, the diffusion fraction and time of mEmerald-LC were quantitatively measured by fluorescence correlation spectroscopy (FCS) (Fig. 2 D) (Shimi *et al.*, 2008; Kochin *et al.*, 2014; Shimi *et al.*, 2016). Because the low expression level of mEmerald-LC was required for FCS measurement, it was stably expressed from a single allele of the *Rosa26* locus with endogenous *Lmna* promotor in WT and G609G/+ MEFs (Fig. S2 A and B). The auto-correlation curve obtained by the signal detection was fitted with fast and slow components (Shimi *et al.*, 2008; Kochin *et al.*, 2014; Shimi *et al.*, 2016). Interestingly, the diffusion coefficient of the fast component, at 37.8% in WT cells was significantly larger than that at 45.0% in G609G/+ cells (Fig. 2 E): ~20.1 ± 1.0 $\mu m^2/s$ and ~12.1 ± 0.8 $\mu m^2/s$ in WT and G609G/+ nuclei, respectively, indicating that PG expression reduced the diffusion speed of mEmerald-LC. These results from FCS measurement could explain in part the slow accumulation of sfGFP-DARPin-LA6 at the rupture sites in G609G/+ cells.

Inhibition of CaaX motif farnesylation increases the localization of LA and PG to the rupture sites

Because the CaaX motifs of pre-LA and PG are farnesylated (Holtz *et al.*, 1989; Sinensky *et al.*, 1994), they are retained at the NE through the hydrophobic interaction with the lipid bilayer of the INM (Holtz *et al.*, 1989; Gelb *et al.*, 2006). Therefore, the localization of farnesylated pre-LA and PG to the rupture sites could be significantly decreased compared to the non-farnesylated forms. To check this possibility, WT and G609G/+ MEFs were treated with DMSO or farnesyltransferase inhibitor (FTI), 3.2 μM lonafarnib for 48 h, and farnesylation levels of pre-LA and PG were determined by immunoblotting and immunofluorescence using specific antibodies directed against pre-LA, mature-LA and PG, which do not cross-react to each other (Fig. S3 A). According to previous studies, the pre-LA antibody appears to have preference for recognizing non-farnesylated pre-LA compared to farnesylated pre-LA by western blotting but not immunofluorescence (Lee *et al.*, 2010; Chang *et al.*, 2012; Yao *et al.*, 2020; Chen *et al.*, 2021). The pre- and mature-LA expression levels were significantly increased and decreased in FTI-treated cells compared to DMSO-treated cells, respectively (Fig. 3 A and S3 B). FTI-treated WT and G609G/+ cells had a higher abundance of LA and PG in the average fluorescence intensity of the nucleoplasmic pool relative to that of the NL (NP/NL ratio) than those treated with DMSO (Fig. 3 B and S3 B). The NP/NL ratio of pre-LA was even higher than that of LA in these FTI-treated cells (Fig. 3 B). These results indicate that LA and PG are increased in the nucleoplasmic pool and/or decreased at the NL by FTI treatment (Fig. 3 B).

These cells were fixed 60 min after laser microirradiation and the localization of LA and PG to the rupture sites was detected by immunofluorescence. LA was localized to the rupture sites in ~59.5%, ~91.4%, ~42.1% and ~73.5% of DMSO-and FTI-treated WT and G609G/+ nuclei, respectively, and pre-LA in ~94.3% and ~76.5% of FTI-treated WT and G609G/+ nuclei (Fig. 3 C). PG was localized to the rupture sites in ~17.6% and

~81.3% of DMSO-and FTI-treated G609G/+ nuclei (Fig. 3 C), as observed in non-treated cells, respectively (Fig. 1 C and D). These results indicate that FTI treatment significantly increases the localization of LA and PG at the rupture sites.

The increase in localization of LA and PG to the rupture sites by FTI treatment was accompanied by an increase in NP/NL ratios (Fig. 3 B and C). Therefore, FTI treatment could also increase the diffusion fraction and time of LA and PG in WT and G609G/+ MEFs. To test this idea, the diffusion fraction and time of mEmerald-LA and PG were measured by FCS. For FCS measurements, mEmerald-LA or PG was stably expressed at a low level from a single allele of the *Rosa26* locus with endogenous *Lmna* promotor in WT and G609G/+ MEFs, followed by the treatment with DMSO or FTI (Fig. S2 A, B and S3 C). As expected, the diffusion coefficient of the fast component in G609G/+ cells was significantly smaller than that in WT cells: ~19.7 ± 1.0 $\mu m^2/s$, ~17.3 ± 0.7 $\mu m^2/s$, ~16.0 ± 0.8 $\mu m^2/s$ and ~17.4 ± 0.7 $\mu m^2/s$ in DMSO- and FTI-treated WT and G609G/+ nuclei, respectively (Fig. 3 E). These results show that PG expression reduced the diffusion speed of mEmerald-LA. The diffusion signals of mEmerald-PG were barely detectable in the nucleoplasm of WT and G609G/+ nuclei treated with DMSO. Instead, the decay signals, which appeared to originate from the NL were detected during FCS measurement because is the lamins are immobile in the NL (Dahl *et al.*, 2006). When WT and G609G/+ cells were treated with the FTI, the diffusion signals were detected by FCS: ~38.3% and ~42.2% of the fast component and ~61.7% and ~57.8% of the slow component in FTI-treated WT and G609G/+ nuclei, respectively (Fig. 3 F). These results indicate that PG becomes diffusible in the nucleoplasm by FTI treatment, and is the likely source of PG localized to the rupture sites.

The second proteolytic cleavage is required for the localization of LA to the rupture sites

Because the localization of PG to the rupture sites was significantly decreased compared to LA (Fig. 1 C and D), the second cleavage site missing from PG could be also involved in increasing pre-LA accumulation. Zmpste24 is involved in endoproteolytic processing of the both the CaaX motif and second cleavage site (Quigley *et al.*, 2013). To test this idea, we employed Zmpste24 knockdown (KD) in WT MEFs by lentivirus-mediated expression of short hairpin RNAs (shRNAs). The expression levels of Zmpste24 and pre-LA were determined in cells expressing shRNAs for the control (Scramble) or Zmpste24 KD (shZmpste24) by immunoblotting and immunofluorescence. The additional 15 C-terminal residues including the CaaX motif remained partially uncleaved by Zmpste24 KD, resulting in the significant increase and decrease in expression level of and pre-LA and mature-LA, as shown as the upper and lower band, respectively (Fig. 4 A). These results are consistent with the previous findings to indicate that Zmpste24 KD inhibits the second proteolytic cleavage (Yu *et al.*, 2013). LA and pre-LA were predominantly localized to the NL, and the NP/NL ratios remained unchanged in Zmpste24-KD cells compared to the control cells (Fig. 4 B and C). This value is similar to that of pre-LA in Zmpste24-KD cells (Fig. 4 C).

These cells were fixed within 60 min after laser microirradiation, and then the localization of LA and pre-LA to the rupture sites were determined by immunofluorescence. LA was localized at the rupture sites in ~75% of the control cells whereas LA and pre-LA were completely absent from the rupture sites in Zmpste24-KD cells (Fig. 4 D and E), indicating that the second cleavage is required for increasing the localization of LA.

Inhibition of farnesylation at the CaaX motif is sufficient for the localization of LA to the rupture sites without the second proteolytic cleavage

Zmpste24 depletion significantly increased pre-LA expression (Fong *et al.*, 2004) (Fig. 5A and B), which is accompanied by farnesylation at the CaaX motif (Lee *et al.*, 2010). Therefore, the inhibition of the farnesylation with FTI could release the pre-LA from the NL, resulting in increasing the localization at the rupture sites. To test this idea, the control and Zmpste24-KD cells were treated with DMSO or FTI as before, and the expression levels and localization of pre-LA and mature-LA were determined by immunoblotting and immunofluorescence (Fig. 5 A and B). As expected, the pre- and mature-LA expression levels were significantly increased and decreased in the control and Zmpste24-KD cells by FTI treatment, respectively (Fig. 5 A and B). Zmpste24 KD also induced the same effect as the FTI treatment, and both of them together had most significant effect among all the combinations (Fig. 5 A and B). The difference in sensitivity between immunoblotting and indirect immunofluorescence of anti-pre-LA antibody (7G11) may be due to specific physical constraints caused by the close proximity of the 7G11 epitope to the farnesylation site rather than the presence of farnesylation (Chang *et al.*, 2012; Casasola *et al.*, 2016; Yao *et al.*, 2020). The combination of pre- and mature-LA was predominantly localized to the NL in these cells (Fig. 5 B). Among them, Zmpste24-KD cells had the lowest NP/NL ratio of pre-LA with DMSO treatment and the highest of mature-LA with FTI treatment (Fig. 5 C and D).

The localization of pre- and mature-LA to the rupture sites was determined by immunofluorescence. Pre-LA was localized to the rupture sites in ~96.9%, ~11.8% and ~77.1% of FTI-treated control nuclei and Zmpste24-KD nuclei with DMSO or FTI

treatment, respectively (Fig. 5 E). Mature-LA was almost undetectable in laser-microirradiated Zmpste24-KD nuclei, and localized to the rupture site in ~56.7% and ~40.6% of DMSO- or FTI-treated control nuclei, respectively (Fig. 5 E). These results indicate that FTI treatment significantly increased the localization of pre-LA but not mature-LA. Therefore, the inhibition of farnesylation at the CaaX motif increases the localization of LA to the rupture sites without the second proteolytic cleavage.

BAF is required for recruiting LA to the rupture sites

BAF binds to the immunoglobulin (Ig)-like fold (Ig-fold) domain in the C-terminal tail region of LA/C (Samson *et al.*, 2018). However, LC but not LA is rapidly recruited to the rupture sites with BAF because LC is more abundant in the nucleoplasm than LA (Kono *et al.*, 2022). It is possible that the slow localization of LA to the rupture sites could be also dependent on BAF within a relatively long-time window. To test this possibility, BAF KD was carried out with two shRNAs (shBAF #1 and #2) (Kono *et al.*, 2022), and the efficiencies of BAF KD were confirmed by immunoblotting and immunofluorescence using WT MEFs expressing shRNA for the control (Scramble) or shBAF #1 and #2 (Fig. 6 A and B). The NP/NL ratio of LA remained unchanged by BAF-KD cells compared to the control cells (Fig. 6 B and C).

These cells were fixed within 60 min after laser microirradiation, and then LA localization was determined by immunofluorescence. As expected, LA was localized to the rupture sites in ~60.6%, 10.0% and ~15.6% of the control and BAF-KD#1 and #2 nuclei, respectively (Fig. 6 D and E), indicating that BAF is required for recruiting LA to the rupture sites.

LA differs from LC in localization to the rupture sites through two specific sequences in the tail region

LA and LC are identical until residue 566 or 568 in human or mouse, respectively (Fig. S4 A). After these residue, LC harbors a unique six amino acid residue whereas LA has 98 or 97 amino acid residues in human or mouse, respectively. Since the LC-specific six amino acid sequence does not contribute to the rapid accumulation of LC at the rupture site (Kono *et al.*, 2022), it is possible that there is the LA-characteristic segment (LACS) that inhibit the rapid accumulation of LA to the rupture sites. To test this idea, LA/C-KO MEFs were transfected with C-terminus truncated mEmerald-LAs, then live-cell imaged after the induction of NE rupture by 405-nm laser microirradiation (Fig. 7 A). mEmerald-LA-S575X had a significant increase in NP/NL ratio compared to mEmerald-LA-FL (Fig. 7 B and C). mEmerald-LA-S575X but not mEmerald-LA-A601X rapidly accumulated within 180 s, indicating that the 26 amino acid sequence of residues 575-600 (LAΔ26) between them is critical for delaying the accumulation (Fig. 7 D and S4 B). Next, because the deletion mutant of the 26 amino acids identified above (mEmerald-LAΔ26) did not accumulate to the rupture site within 180 s, further truncation was performed at the C-terminal side of mEmerald-LAΔ26 (Fig.7 A). The NP/NL ratio of mEmerald-LAΔ26 remained unchanged until the C-terminal truncation at residue 627 (mEmerald-LAΔ26-F627X) compared to the mEmerald-LA-FL (Fig. S4 C-E and S4 E), indicating that residues 627-643 are critical for inhibiting the accumulation. We therefore designated LAΔ26 as LA-characteristic sequence-1 (LACS1) and the 17 amino acid sequence identified later (627-643) as LACS2.

Discussion

A-type lamins are recruited to sites of NE rupture to repair the NL (Denais *et al.*, 2016; Raab *et al.*, 2016; Kono *et al.*, 2022). We previously showed that the recruitment of LC was significantly earlier than that of LA and was not attributable to the unique six amino acid segment at the C-terminus following the amino acid sequence shared between them (Kono *et al.*, 2022). In this study, we analyze the pre-LA tail region extended from the unique segment, and Fig. 8 summarizes our current findings following our previous study. The CaaX motif, the second proteolytic cleavage site and two LACSs of the LA tail region determine the abundance of the nucleoplasmic pool. Because of the recruitment from the nucleoplasm to the rupture sites, the processing and binding of these regulatory segments are likely to be rate-limiting steps for the localization kinetics at the rupture sites.

We use immortalized G609G/+ MEFs to analyze the CaaX motif and the second cleavage site of pre-LA with respect to the localization at the rupture sites. Unlike HGPS patient cells, G609G/+ cells do not exhibit spontaneous NE rupture, which could be due to the immortalization process with SV40 large T antigen. In oncogene-induced senescence, DNA protrusion from the nucleus and the leakage of nuclear contents are coupled to the loss of LB1 (Shimi *et al.*, 2011; Ivanov *et al.*, 2013; Dou *et al.*, 2015). LB1 expression could also decrease when HGPS patient cells become prematurely senescent (Scaffidi and Misteli, 2005). Therefore, spontaneous NE rupture might be induced by the HGPS mutation because of premature senescence. Instead of spontaneous NE rupture, we find that after forced NE rupture induced by AFM indentation, the nuclear reentry of NLS-sfCherry is significantly slow in G609G/+ cells compared to WT cells. Our comparison between WT and G609G/+ cells shows that PG is not only slower in localizing to the rupture sites than LA but also delays LA localization and LC

accumulation probably because PG stably interacts with LA and LC to form a regularly aligned filaments in the NL (Dahl *et al.*, 2006). These results suggest that the HGPS mutation would impair the repair of NE rupture rather than the structural integrity of the NE.

When farnesylation at the CaaX motif of LA and PG is inhibited by FTI treatment, pre-LA and pre-PG are increased in the nucleoplasm and localized to the rupture sites, indicating that the farnesylation process limits the localization to the rupture sites regardless of the second proteolytic cleavage of LA. Furthermore, Zmpste24 KD blocks the second cleavage, leading to the complete inhibition of pre-LA localization to the rupture sites, and the effect of Zmpste24 KD on the localization is rescued by FTI treatment. These results strongly suggest that the majority of pre-LA molecules are farnesylated by Zmpste24 KD and that the farnesylated form cannot localize to the rupture sites.

Our previous and current studies indicate that LA and LC are recruited to the rupture sites with BAF (Kono *et al.*, 2022). Despite this common mechanism for the recruitment between them, the recruitment of LA is significantly slower that of LC because LC is more abundant in the nucleoplasm than LA (Kono *et al.*, 2022). This sequential order is positively correlated with the molecular exchange rates in the NL (Broers *et al.*, 1999; Dahl *et al.*, 2006), suggesting that BAF facilitates the assembly of LA and LC into the NL to maintain nuclear structure during interphase. To support this idea, our and other's results indicate that BAF KD reduces LA in the NL (Haraguchi *et al.*, 2007; Haraguchi *et al.*, 2008).

Apart from the farnesylation at the CaaX motif and the inhibition of the second proteolytic cleavage of pre-LA, we find that LACS1 and LACS2 in the tail region delay

the localization at the rupture sites. Because the truncation of LACS1 significantly increases the nucleoplasmic pool, LA appears to be retained at the NL longer than LC through LACS1. It is possible that LACS1 is involved in the retention by the formation of LA filament (e.g. polymerization) in the NL or the interaction with NE components including INM proteins and SUN1/2. On the other hand, LACS2 could independently inhibit LA localization to the rupture sites and/or assist LACS1 function for the retention. In addition to the chromatin-binding domain (CBD) of LA/C, residues 396-430,which was determined using the LC tail region (Taniura *et al.*, 1995), these LACSs might bind to histones as LA-specific CBDs (Schibler *et al.*, 2023).

In the context of HGPS, the farnesylation at the CaaX motif and lack of the second proteolytic cleavage site significantly reduce the nucleoplasmic pol of PG, leading to the slow localization of PG to the rupture sites compared to LA. This molecular mechanism could be also critical for their access to active enhancers in the nuclear interior (Ikegami *et al.*, 2020). The presence of PG can lead to increased NE instability but we do not observe spontaneous NE rupture in G609G/+ cells. Nevertheless, our findings implicate pathological significance of the defective repair of the NL as indicated by the slow localization kinetics of PG at the rupture sites. The therapeutic effect of FTI treatment appears to rescue from the repair defect by targeting the farnesylation at the CaaX motif of PG. Therefore, the induction of spontaneous NE rupture and the rescuing with FTI treatment need validating using the mouse model of HGPS in future studies.

Materials and methods

Plasmid construction

Two different NLSs derived from SV40 large T antigen (NLS^{SV40}; PKKKRKV) and c-Myc (NLS^{Myc}; PAAKRVKLD) from pCDH-NLS^{SV40}-sfCherry-NLS^{Myc}-Blast (Kono *et al.*, 2022) were ligated to pCDH-CMV-MCS-EF1-Hygro (plasmid #CD515B-1, System Biosciences) using the Ligation-Convenience Kit (Nippon Gene) and designated as pCDH-NLS^{SV40}-sfCherry-NLS^{Myc}-Hygro. The annealed oligonucleotides to express shRNAs (ZmpSte24, TRCN0000366641; BAF#1, TRCN0000124958; BAF#2, TRCN0000124955; Table S2, Broad Institute) was ligated into pLKO.3-blast (Kono *et al.*, 2022) using the Ligation-Convenience Kit. The pX459-sfCherry CRISPR-Cas9 vector were generated from pSpCas9(BB)-2A-Puro (pX459) V2.0 (Addgene plasmid # 62988 ; http://n2t.net/addgene:62988 ; RRID:Addgene_62988; a gift from Feng Zhang). The annealed oligonucleotides to express single-guide RNA (sgRNA) against the *Rosa26* target sequence (Chu *et al.*, 2015) was ligated into pX459-sfCherry using the Ligation-Convenience Kit and designated as pX459-sfCherry-sgRosa26-1.

We cloned a 1.6 kb genomic region upstream from start codon of mouse *Lmna* as the endogenous promoter (-1407 to +249 bp from transcription start site) using PrimeSTAR HS DNA Polymerase (Takara). Primers used in this study are listed in Table S2. Mouse genomic DNA was extracted from cells by Proteinase K (Fungal; Invitrogen) digestion according to the standard protocol and used for a PCR template. The CMV promoter of mEmerald-C1 (Addgene plasmid # 53975 ; http://n2t.net/addgene:53975 ; RRID:Addgene_53975; a gift from Michael Davidson) was replaced by a *Lmna* promoter using the In-Fusion HD Cloning Kit (Clontech) and designated as pLmna-mEmerald-C1. The mouse pre-LA cDNA was amplified from pPyCAG-LA-IP (Guo *et al.*, 2014) using the KOD One PCR Master Mix -Blue- (Toyobo), cloned into pLmna-mEmerald-C1 using the In-Fusion, and designated as pLmna-Em-LA. The mouse PG cDNA was generated by PrimeSTAR Max DNA Polymerase (Takara) to skip 150 bp, closed by In-Fusion HD, and designated as pLmna-Em-PG. The amino acid truncation mutants were generated by PCR mutagenesis using PrimeSTAR Max or PrimeSTAR HS DNA Polymerase. The LACS1 deletion mutant (Δ26) was generated using PrimeSTAR Max to skip 78 bp, and closed by In-Fusion HD. The pLmna-Em-LA and pLmna-Em-PG expression cassettes were amplified by the KOD One, fused with bGHpA amplified from LSL-Cas9-Rosa26TV

(Addgene plasmid # 61408 ; http://n2t.net/addgene:61408 ; RRID:Addgene_61408; a gift from Feng Zhang) and *Pac* I/*Sma* I digested LSL-Cas9-Rosa26TV by In-Fusion HD, and designated as pLmna-Em-LA-R26Neo and pLmna-Em-PG-R26Neo, respectively. The mouse LC cDNA was also generated by KOD One PCR and In-Fusion HD and designated as pLmna-Em-LC-R26Neo.

Cell culture

MEFs isolated from WT and heterozygous c.1827C>T mutant (*Lmna*$^{G609G/+}$, G609G/+) embryos at embryonic day 13.5 were generous gifts from Carlos López-Otín, Universidad de Oviedo (Lopez-Mejia *et al.*, 2011; Osorio *et al.*, 2011). Primary MEFs were cultured in modified DMEM (high glucose; Nacalai Tesque) containing 10% FBS (qualified; Thermo Fisher), 4 mM L-glutamine, 100U/mL penicillin and 100 μg/mL streptomycin (Sigma-Aldrich), and 20 mM 2-[4-(2-Hydroxyethyl)-1-piperazinyl] ethanesulfonic acid (HEPES; Nacalai Tesque) at 37°C in a humidified multi-gas incubator with 3% O_2/5% CO_2 (MCO-5M, Sanyo/Panasonic Healthcare). Cells were immortalized by transduction with a retrovirus expressing SV40 large T antigen from pBABE-puro largeTcDNA (Addgene plasmid # 14088 ; http://n2t.net/addgene:14088 ; RRID:Addgene_14088; a gift from William Hahn) as previously described (Shimi *et al.*, 2015). After selection with 2 μg/ml puromycin (InvivoGen) for 4 d, immortalized WT and G609G/+ cells were cultured in growth medium without HEPES at 37°C in a humidified chamber with 5% CO_2.

Lentiviral transduction

For lentivirus-mediated stable introduction of NLS^{SV40}-sfCherry-NLS^{Myc}, we followed the methods described previously (Kono *et al.*, 2022). Briefly, pVSV-G (PT3343-5, Clontech) and psPAX2 (Addgene plasmid #12260; http://n2t.net/addgene:12260; RRID:Addgene_12260; a gift from Didier Trono), together with a pCDH vector (pCDH-NLS^{SV40}-sfCherry-NLS^{Myc}-Blast, pCDH-NLS^{SV40}-sfCherry-NLS^{Myc}-Hygro or pCDH-sfGFP-DARPin-LA6-Hygro) in a 1:3:4 weight ratio of each plasmid was transfected into ~80% confluent 293T cells (CRL-3216, ATCC) using Lipofectamine 3000 following the manufacturer's instructions for lentivirus production. One day after the transfection, the medium was replaced with fresh medium, which was harvested at 48 h after transfection.

For virus infection, MEFs were incubated with the virus-containing culture supernatants with 4 μg/mL polybrene (Nacalai Tesque) for 24 h. Infected cells were selected by incubation in medium containing 3 μg/mL blasticidin S or 200 μg/mL hygromycin B Gold (InvivoGen) for 4 d.

Live-cell imaging and NE rupture induction by laser microirradiation

Culture medium was replaced with FluoroBrite (Thermo Fisher) containing 10% FBS, 4 mM L-glutamine, 100U/mL penicillin and 100 μg/mL streptomycin. For laser-microirradiation and image collection, cells were set onto a heated stage (37°C; Tokai Hit) with a CO_2-control system (Tokken) on a confocal microscope (FV1000, Olympus) with a 60× PlanApo N (NA 1.4) oil lens operated by built-in software FLUOVIEW ver. 4.2 (Olympus). All live-cell images were collected using a main scanner (4% 488-nm laser transmission; 30% 543-nm laser transmission; 2 μs/pixel; 512×512 pixels; pinhole 100 μm; 6× zoom; ~10 s/frame). After the first image was acquired, a 2 μm diameter spot was laser-microirradiated using a second scanner at 100% power of 405-nm laser transmission (40 μs/pixel; approximately 780 μW) for 10 s while the images were collected with another scanner.

Fiji software (ImageJ) ver. 1.53v (National Institute of Health) was used for measuring max intensity in the region of interest after Gaussian filtering with $\sigma = 2.0$ over time. Fluorescence intensity was normalized by each of the initial intensity in the laser-microirradiated region. CellProfiler ver. 3.1.9 (Broad Institute) with the NP_NL_intensity_live pipeline (uploaded on GitHub; http://github.com/Kimura-Lab/Kono-et-al.-2023) (Kono *et al.*, 2022) were used for measuring mean intensity of mEmerald-LA mutants and mEmerald-LC in the NP and the NL. Briefly, after the nuclear region was recognized by the nuclear localization of NLS-sfCherry, 3 pixels (207 nm) and more than 10 pixels (690 nm) inside from the rim of nuclear region were regarded as the NL and the NP, respectively, and then the mean intensity of each section was measured. All images were processed in Photoshop ver. 24 (Adobe) for cropping and brightness/contrast adjustment when applicable.

Indirect immunofluorescence and microscopy

Primary antibodies used for indirect immunofluorescence were mouse monoclonal anti-LA (1:250; 4A58, sc-71481, Santa Cruz), rat monoclonal anti-pre-LA (1:1,000; 7G11; MABT345, EMD Millipore; (Lee *et al.*, 2010)), mouse monoclonal anti-mature-LA (1:8,000; 4A4-A4, 14-9848-82, Invitrogen; (Roblek *et al.*, 2010)), rabbit polyclonal anti-progerin (1:1000; generated by the Nourshargh laboratory using a peptide immunogen of murine progerin and standard immunization procedures; (Santiago-Fernández *et al.*, 2019; Marcos-Ramiro *et al.*, 2021; Sánchez-López *et al.*, 2021)) and rabbit monoclonal anti-BANF1/BAF (1:200; EPR7668; ab129184, Abcam). The secondary antibodies used were Alexa Fluor 488-donkey anti-mouse immunoglobulin G (IgG), Alexa Fluor 488-donkey anti-rabbit IgG (1:2,000; A21202 and 1:2,000; A21206, respectively, Thermo Fisher), Cy5-donkey anti-mouse IgG and Cy5-goat anti-rat IgG (1:2,000; 715-175-151 and 1:2,000; 712-175-153, respectively, Jackson ImmunoResearch).

Cells were grown on 35 mm Glass Based Dishes which have a cover glass with a grid pattern (IWAKI) and fixed after laser-microirradiation with 4% PFA (Electron Microscopy Sciences) containing 0.1% Triton X-100 (Nacalai Tesque) for 15 min, followed by permeabilization using 0.1% Triton X-100 in PBS for 10 min and then blocking with Blocking One-P (Nacalai Tesque) for 30 min. Cells were incubated with primary antibodies overnight at 4°C, washed with 10% Blocking One-P in PBS, and incubated with secondary antibodies for 1 h at RT. DNA was stained with Hoechst 33342 (0.5 μg/mL; Thermo Fisher). For Fig. S1 A, cells were fixed with 4% PFA for 15 min, followed by permeabilization using 0.1% Triton X-100 in PBS for 10 min and then blocking with Blocking One-P for 30 min. The RFP-Booster Alexa Fluor 568 (alpaca monoclonal anti-RFP Nanobody; 1:1000; rb2AF568, ChromoTek) was used to amplify the signal of NLS-sfCherry.

Confocal fluorescence images were obtained using a confocal microscope FV1000 with a 60× PlanApo N (NA 1.4) oil lens (3.0% 405-nm laser transmission; 3.1-11.1% 488-nm laser transmission; 5.0% 543-nm laser transmission; 1.0-4.0% 633-nm laser transmission; 2 μs/pixel; 512×512 pixels; pinhole 100 μm). CellProfiler with the NP_NL_intensity_fixed pipeline (uploaded on GitHub; http://github.com/Kimura-Lab/Kono-et-al.-2023) were used for measuring mean intensity of lamins in the NP and the NL. Briefly, after the nuclear region was recognized by the DNA, 3 pixels (207 nm) and more than 10 pixels (690 nm) inside from the rim of nuclear region were regarded as

the NL and the NP, respectively, and then the mean intensity of each section was measured. All images were processed in Photoshop ver. 24 for cropping and brightness/contrast adjustment when applicable.

Induction of mechanical NE rupture by atomic force microscopy (AFM)

Culture medium was replaced with Leibovitz's L-15 medium (no phenol red; Thermo Fisher) containing 10% FBS, 2 mM L-glutamine, 100U/mL penicillin and 100 μg/mL streptomycin. JPK NanoWizard 4 BioAFM (Bruker) incorporated into an inverted fluorescence microscope (Eclipse Ti2, Nikon) with EM-CCD camera (iXon Ultra 888, Andor) and light source (X-Cite XYLIS, Excelitas) was used for single-cell compression. Cantilever (TL-CONT, Nanosensors; spring constant approximately 0.2 N/m) with a 100 μm glass bead (BZ-01, As-One) was used for NE rupture. Cells expressing NLS-sfCherry were set onto a heated stage (37°C) and the first fluorescent image of NLS-sfCherry was obtained before the rupture using a TRITC filter and NIS-Elements BR (Nikon). Next, the bead was approached on the top of the cell surface with 2 nN setpoint and then forced down for 5 μm. After waiting for 10 s, the cantilever was retracted. Within 10 s after the retraction, time-lapse imaging was started with 30 s exposure time every 30 s for 5 min.

Chemicals

As a selective farnesyltransferase inhibitor (FTI), lonafarnib (SCH66336; Merck) was dissolved in dimethylsulfoxide (DMSO; Nacalai Tesque) and added to the cells with one daily dose of 3.2 μM for 2 days. For controls in all experiments, an equal volume of vehicle (0.1% DMSO) was added.

Immunoblotting

For immunoblotting, we followed the methods described previously (Kono et al., 2022). Briefly, primary antibodies used for immunoblotting were mouse monoclonal anti-LA/C (1:5,000-20,000; 3A6-4C11, 14-9847-82, eBioscience), rat monoclonal anti-pre-LA (1:1,000; 7G11), mouse monoclonal anti-mature-LA (1:2,500; 4A4-A4), rabbit polyclonal anti-progerin (1:1,000; Nourshargh lab), rabbit monoclonal anti-BANF1/BAF (1:500; EPR7668, Abcam), anti-β-Actin (1:2,000; AC-15, sc-69879, Santa

Cruz) and anti-GAPDH (1:5,000; 6C5, sc-32233, Santa Cruz). The secondary antibodies used were anti-mouse IgG HRP-linked whole Ab sheep (1:10,000; NA931, Amersham), anti-rabbit IgG HRP-linked F(ab')$_2$ fragment donkey (1:10,000; NA9340, Amersham) and HRP-donkey anti-rat IgG (H+L) (1:10,000; 712-035-150, Jackson ImmunoResearch).

Rosa26-targeted gene knock-in

The pLmna-Em-preLA-R26Neo, pLmna-Em-PG-R26Neo and pLmna-Em-LC-R26Neo were linearized by the *Kpn* I (Takara) and purified by phenol/chloroform extraction and ethanol precipitation. Cells were transfected with appropriate plasmids using Lipofectamine 3000 (Thermo Fisher) by reverse transfection as previously described (Kono *et al.*, 2022). Briefly, the DNA-lipid complex (3 μg linearized *Rosa26* targeting vectors : 2 μg pX459-sfCherry-sgRosa26-1 : 7.5 μL Lipofectamine 3000 in 250 μL Opti-MEM; Thermo Fisher) was added to 1.62×10^5 cells as they were seeding onto a 35 mm dish with 2 mL of growth medium. One day after the transfection, the medium was replaced with fresh medium. Two days after the transfection, cells were selected by incubation in medium containing 400 μg/mL G-418 disulfate aqueous solution (Nacalai Tesque) for 7 d.

Fluorescence Correlation Spectroscopy (FCS)

FCS measurements were all performed at 25°C with an LSM780 confocal microscope (Carl Zeiss) as described previously (Shimi *et al.*, 2008; Park *et al.*, 2015; Shimi *et al.*, 2016). FCS setups using the LSM780 microscope consisted of a continuous-wave Ar^+ laser (25 mW), a water-immersion objective (C-Apochromat, ×40/1.2 NA; Carl Zeiss), and a GaAsP multichannel spectral detector (Quasar; Carl Zeiss). Fluorescent protein of mEmerald was excited with the 488-nm laser line with a minimal laser power (0.5%) to allow an optimal signal-to-noise ratio. Diameter of pinhole was adjusted to 34 μm (1 Airy unit) for the 488-nm laser. Emission fluorescence was detected at 500–550 nm in the green channel. The structure parameter and detection volume were calibrated using Rhodamine-6G (Sigma-Aldrich) solution with diffusion coefficient (280 $\mu m^2/s$; 25°C in water) before cell experiment. For live cell analysis, three positions of FCS measurement were selected in the nuclei of cells excluding the nucleoli. For FCS measurements, measuring time and repetition were set to 10 s and 5 times, respectively. The first of five

repetitions were considered prebleach, and then four repetitions were used for further analysis. FCS data were analyzed with analytical software installed in the ZEN 2012 SP5 FP1 (black) acquisition software (Carl Zeiss) (Park *et al.*, 2015; Shimi *et al.*, 2016). Briefly, all measured fluorescence auto-correlation functions (FAFs) from live cells were globally fitted by the ConfoCor3 software installed on LSM780 system using fitting models considering three-dimensional free diffusion with a Gaussian laser profile, including a triplet component to estimate the diffusion coefficient.

Generation of the ZmpSte24- and BAF-KD MEFs

MEFs expressing shRNAs of anti-ZmpSte24 and anti-BAF were generated through lentiviral transduction. KD by shRNA expression was carried out by Lentivirus transduction (see the section on Lentiviral transduction above) and 3 d selection with 3 µg/mL blasticidin S Gold for pLKO.3-blast.

Statistical analyses

Unless mentioned otherwise, all plots showed mean values ± SEM (error bars). Fisher's exact test was performed to analyze the categorical data using EZR on R commander ver. 1.61 (programmed by Yoshinobu Kanda) (Kanda, 2013). The mixed effect model fit by restricted maximum likelihood (REML) was performed to analyze the interaction between group and time using the *lme4* (Bates *et al.*, 2015) and the *lmerTest* (Kuznetsova *et al.*, 2017) packages in EZR, where cell's id was set as a random effect, while group and time as fixed effects. The interaction between group and time (group × time) was also set as a fixed effect. The Welch's t-test or the Welch's one-way ANOVA followed by the Games–Howell post-hoc test was performed to single or multiple comparison, respectively. Statistic codes for R ver. 4.2.2 and a modified R commander for EZR 1.61 are uploaded on GitHub (http://github.com/Kimura-Lab/Kono-et-al.-2023). Significance was determined if $P < 0.05$.

Supplemental material

Table S1 shows the phenotype characterization in WT and G609G/+ MEFs by immunofluorescence. Table S2 shows oligonucleotide sequences used in this study. Fig. S1 shows the immunofluorescence of WT and G609G/+ MEFs for phenotype characterization, and localization of LA and PG to NE rupture site at 30 and 120 min after laser microirradiation. Fig. S2 shows the *Rosa26* knocked-in cells expressing A-type lamins under Lmna promoter for FCS analysis. Fig. S3 shows the immunofluorescence, immunoblotting and diffusion fraction in FTI-treated WT and G609G/+ MEFs. Fig. S4 shows the differences between LA and LC amino acid sequence, and dynamics of LA mutants at the rupture sites, and the fluorescence intensities in the NP to the NL ratio of mEmerald-LA mutants by live-cell imaging.

Acknowledgments

We would like to thank Prof. Carlos López-Otín (Universidad de Oviedo) for providing us with the primary MEFs isolated from WT and *Lmna* c.1827C>T mutant (*Lmna*$^{G609G/+}$ and *Lmna*$^{G609G/G609G}$) embryos. We thank Biomaterials Analysis Division, Open Facility Center (OFC) of Tokyo Institute of Technology for nucleotide sequencing and sharing research equipment, especially Carl Zeiss ElyraS1/Airyscan/LSM780 is shared in MEXT Project Grant no. JPMXS0440200021. We also thank the Cellular Imaging Core Facility at the ConveRgence mEDIcine research cenTer (CREDIT), Asan Medical Center for technical support. The generation and validation of the anti-murine progerin antibody was funded by the Wellcome Trust (098291/Z/12/Z to S. Nourshargh) and by the British Heart Foundation (FS/IBSRF/22/25121 to L. Rolas). We also acknowledge the R statistic code generated by Shinsuke Hatano (Ryukoku University). We also thank all members of the Kimura lab at Tokyo Institute of Technology for advice and discussions. This work was supported by JSPS KAKENHI Grant Numbers JP20KK0158 (to T. Shimi, Y. Kono and H. Kimura), JP20K06617 (to T. Shimi), and JP18H05527 and JP21H04764 (to H. Kimura). Y. Kono was an academy scholar at the Specialized Academy for Cell Science (Ohsumi-juku) of the Tokyo Tech Organization for Fundamental Research (OFR). The authors declare no competing financial interests.

Author contributions

T. Shimi conceived the project. Y. Kono designed, performed and interpreted experiments. C.G. Pack performed FCS experiments. T. Ichikawa performed AFM experiments. A. Komatsubara performed image analysis. M. Golding, L. Rolas and S. Nourshargh generated, characterized, and provided the anti-murine progerin antibody. S.A. Adam, O. Medalia and R.D. Goldman provided advice and scientific discussion. Y. Kono, C.G. Pack, T. Ichikawa and T. Shimi drafted the manuscript. S.A. Adam, R.D. Goldman, and H. Kimura edited the manuscript. T. Shimi, S.A. Adam, T. Fukuma, H. Kimura and R.D. Goldman supervised the experiments.

References

Bates, D., Mächler, M., Bolker, B.M., and Walker, S.C. (2015). Fitting Linear Mixed-Effects Models Using lme4. Journal of Statistical Software *67*, 1-48.

Biamonti, G., Giacca, M., Perini, G., Contreas, G., Zentilin, L., Weighardt, F., Guerra, M., Della Valle, G., Saccone, S., Riva, S., and Falaschi, A. (1992). The gene for a novel human lamin maps at a highly transcribed locus of chromosome 19 which replicates at the onset of S-phase. Mol Cell Biol *12*, 3499-3506.

Boyartchuk, V.L., Ashby, M.N., and Rine, J. (1997). Modulation of Ras and a-factor function by carboxyl-terminal proteolysis. Science *275*, 1796-1800.

Broers, J.L.V., Machiels, B.M., van Eys, G.J.J.M., Kuijpers, H.J.H., Manders, E.M.M., van Driel, R., and Ramaekers, F.C.S. (1999). Dynamics of the nuclear lamina as monitored by GFP-tagged A-type lamins. J Cell Sci *112 (Pt 20)*, 3463-3475.

Casasola, A., Scalzo, D., Nandakumar, V., Halow, J., Recillas-Targa, F., Groudine, M., and Rincón-Arano, H. (2016). Prelamin A processing, accumulation and distribution in normal cells and laminopathy disorders. Nucleus *7*, 84-102.

Chang, S.Y., Hudon-Miller, S.E., Yang, S.H., Jung, H.J., Lee, J.M., Farber, E., Subramanian, T., Andres, D.A., Spielmann, H.P., Hrycyna, C.A., Young, S.G., and Fong, L.G. (2012). Inhibitors of protein geranylgeranyltransferase-I lead to prelamin A accumulation in cells by inhibiting ZMPSTE24. J Lipid Res *53*, 1176-1182.

Chen, N.Y., Kim, P., Weston, T.A., Edillo, L., Tu, Y., Fong, L.G., and Young, S.G. (2018). Fibroblasts lacking nuclear lamins do not have nuclear blebs or protrusions but nevertheless have frequent nuclear membrane ruptures. Proc Natl Acad Sci U S A *115*, 10100-10105.

Chen, N.Y., Yang, Y., Weston, T.A., Belling, J.N., Heizer, P., Tu, Y., Kim, P., Edillo, L., Jonas, S.J., Weiss, P.S., Fong, L.G., and Young, S.G. (2019). An absence of lamin B1 in migrating neurons causes nuclear membrane ruptures and cell death. Proc Natl Acad Sci U S A *116*, 25870-25879.

Chen, X., Yao, H., Kashif, M., Revêchon, G., Eriksson, M., Hu, J., Wang, T., Liu, Y., Tüksammel, E., Strömblad, S., Ahearn, I.M., Philips, M.R., Wiel, C., Ibrahim, M.X., and Bergo, M.O. (2021). A small-molecule ICMT inhibitor delays senescence of Hutchinson-Gilford progeria syndrome cells. Elife *10*.

Chu, V.T., Weber, T., Wefers, B., Wurst, W., Sander, S., Rajewsky, K., and Kühn, R. (2015). Increasing the efficiency of homology-directed repair for CRISPR-Cas9-induced precise gene editing in mammalian cells. Nat Biotechnol *33*, 543-548.

Corrigan, D.P., Kuszczak, D., Rusinol, A.E., Thewke, D.P., Hrycyna, C.A., Michaelis, S., and Sinensky, M.S. (2005). Prelamin A endoproteolytic processing in vitro by recombinant Zmpste24. Biochem J *387*, 129-138.

Crisp, M., Liu, Q., Roux, K., Rattner, J.B., Shanahan, C., Burke, B., Stahl, P.D., and Hodzic, D. (2006). Coupling of the nucleus and cytoplasm: role of the LINC complex. J Cell Biol *172*, 41-53.

Dahl, K.N., Scaffidi, P., Islam, M.F., Yodh, A.G., Wilson, K.L., and Misteli, T. (2006). Distinct structural and mechanical properties of the nuclear lamina in Hutchinson-Gilford progeria syndrome. Proc Natl Acad Sci U S A *103*, 10271-10276.

De Sandre-Giovannoli, A., Bernard, R., Cau, P., Navarro, C., Amiel, J., Boccaccio, I., Lyonnet, S., Stewart, C.L., Munnich, A., Le Merrer, M., and Lévy, N. (2003). Lamin a truncation in Hutchinson-Gilford progeria. Science *300*, 2055.

De Vos, W.H., Houben, F., Kamps, M., Malhas, A., Verheyen, F., Cox, J., Manders, E.M.M., Verstraeten, V.L.R.M., van Steensel, M.A.M., Marcelis, C.L.M., van den Wijngaard, A., Vaux, D.J., Ramaekers, F.C.S., and Broers, J.L.V. (2011). Repetitive disruptions of the nuclear envelope invoke temporary loss of cellular compartmentalization in laminopathies. Hum Mol Genet *20*, 4175-4186.

Denais, C.M., Gilbert, R.M., Isermann, P., McGregor, A.L., te Lindert, M., Weigelin, B., Davidson, P.M., Friedl, P., Wolf, K., and Lammerding, J. (2016). Nuclear envelope rupture and repair during cancer cell migration. Science *352*, 353-358.

Dou, Z., Xu, C., Donahue, G., Shimi, T., Pan, J.A., Zhu, J., Ivanov, A., Capell, B.C., Drake, A.M., Shah, P.P., Catanzaro, J.M., Ricketts, M.D., Lamark, T., Adam, S.A., Marmorstein, R., Zong, W.X., Johansen, T., Goldman, R.D., Adams, P.D., and Berger, S.L. (2015). Autophagy mediates degradation of nuclear lamina. Nature *527*, 105-109.

Earle, A.J., Kirby, T.J., Fedorchak, G.R., Isermann, P., Patel, J., Iruvanti, S., Moore, S.A., Bonne, G., Wallrath, L.L., and Lammerding, J. (2020). Mutant lamins cause nuclear envelope rupture and DNA damage in skeletal muscle cells. Nat Mater *19*, 464-473.

Eriksson, M., Brown, W.T., Gordon, L.B., Glynn, M.W., Singer, J., Scott, L., Erdos, M.R., Robbins, C.M., Moses, T.Y., Berglund, P., Dutra, A., Pak, E., Durkin, S., Csoka, A.B., Boehnke, M., Glover, T.W., and Collins, F.S. (2003). Recurrent de novo point mutations in lamin A cause Hutchinson-Gilford progeria syndrome. Nature *423*, 293-298.

Foisner, R., and Gerace, L. (1993). Integral Membrane-Proteins of the Nuclear-Envelope Interact with Lamins and Chromosomes, and Binding Is Modulated by Mitotic Phosphorylation. Cell *73*, 1267-1279.

Fong, L.G., Ng, J.K., Meta, M., Coté, N., Yang, S.H., Stewart, C.L., Sullivan, T., Burghardt, A., Majumdar, S., Reue, K., Bergo, M.O., and Young, S.G. (2004). Heterozygosity for Lmna deficiency eliminates the progeria-like phenotypes in Zmpste24-deficient mice. Proc Natl Acad Sci U S A *101*, 18111-18116.

Gelb, M.H., Brunsveld, L., Hrycyna, C.A., Michaelis, S., Tamanoi, F., Van Voorhis, W.C., and Waldmann, H. (2006). Therapeutic intervention based on protein prenylation and associated modifications. Nat Chem Biol *2*, 518-528.

Gerace, L., and Blobel, G. (1980). The nuclear envelope lamina is reversibly depolymerized during mitosis. Cell *19*, 277-287.

Gerace, L., Blum, A., and Blobel, G. (1978). Immunocytochemical localization of the major polypeptides of the nuclear pore complex-lamina fraction. Interphase and mitotic distribution. J Cell Biol *79*, 546-566.

Guo, Y., Kim, Y., Shimi, T., Goldman, R.D., and Zheng, Y. (2014). Concentration-dependent lamin assembly and its roles in the localization of other nuclear proteins. Mol Biol Cell *25*, 1287-1297.

Halfmann, C.T., Sears, R.M., Katiyar, A., Busselman, B.W., Aman, L.K., Zhang, Q., O'Bryan, C.S., Angelini, T.E., Lele, T.P., and Roux, K.J. (2019). Repair of nuclear ruptures requires barrier-to-autointegration factor. J Cell Biol *218*, 2136-2149.

Haraguchi, T., Kojidani, T., Koujin, T., Shimi, T., Osakada, H., Mori, C., Yamamoto, A., and Hiraoka, Y. (2008). Live cell imaging and electron microscopy reveal dynamic processes of BAF-directed nuclear envelope assembly. J Cell Sci *121*, 2540-2554.

Haraguchi, T., Koujin, T., Osakada, H., Kojidani, T., Mori, C., Masuda, H., and Hiraoka, Y. (2007). Nuclear localization of barrier-to-autointegration factor is correlated with progression of S phase in human cells. J Cell Sci *120*, 1967-1977.

Höger, T.H., Zatloukal, K., Waizenegger, I., and Krohne, G. (1990). Characterization of a second highly conserved B-type lamin present in cells previously thought to contain only a single B-type lamin. Chromosoma *99*, 379-390.

Holtz, D., Tanaka, R.A., Hartwig, J., and McKeon, F. (1989). The CaaX motif of lamin A functions in conjunction with the nuclear localization signal to target assembly to the nuclear envelope. Cell *59*, 969-977.

Ikegami, K., Secchia, S., Almakki, O., Lieb, J.D., and Moskowitz, I.P. (2020). Phosphorylated Lamin A/C in the Nuclear Interior Binds Active Enhancers Associated with Abnormal Transcription in Progeria. Dev Cell *52*, 699-713 e611.

Ivanov, A., Pawlikowski, J., Manoharan, I., van Tuyn, J., Nelson, D.M., Rai, T.S., Shah, P.P., Hewitt, G., Korolchuk, V.I., Passos, J.F., Wu, H., Berger, S.L., and Adams, P.D. (2013). Lysosome-mediated processing of chromatin in senescence. J Cell Biol *202*, 129-143.

Ivanovska, I.L., Tobin, M.P., Bai, T., Dooling, L.J., and Discher, D.E. (2023). Small lipid droplets are rigid enough to indent a nucleus, dilute the lamina, and cause rupture. J Cell Biol *222*.

Kanda, Y. (2013). Investigation of the freely available easy-to-use software 'EZR' for medical statistics. Bone Marrow Transplant *48*, 452-458.

Kim, P.H., Chen, N.Y., Heizer, P.J., Tu, Y., Weston, T.A., Fong, J.L.C., Gill, N.K., Rowat, A.C., Young, S.G., and Fong, L.G. (2021). Nuclear membrane ruptures underlie the vascular pathology in a mouse model of Hutchinson-Gilford progeria syndrome. JCI Insight *6*.

Kittisopikul, M., Shimi, T., Tatli, M., Tran, J.R., Zheng, Y., Medalia, O., Jaqaman, K., Adam, S.A., and Goldman, R.D. (2021). Computational analyses reveal spatial relationships between nuclear pore complexes and specific lamins. J Cell Biol *220*.

Kochin, V., Shimi, T., Torvaldson, E., Adam, S.A., Goldman, A., Pack, C.G., Melo-Cardenas, J., Imanishi, S.Y., Goldman, R.D., and Eriksson, J.E. (2014). Interphase phosphorylation of lamin A. J Cell Sci *127*, 2683-2696.

Kono, Y., Adam, S.A., Sato, Y., Reddy, K.L., Zheng, Y., Medalia, O., Goldman, R.D., Kimura, H., and Shimi, T. (2022). Nucleoplasmic lamin C rapidly accumulates at sites of nuclear envelope rupture with BAF and cGAS. J Cell Biol *221*.

Kuznetsova, A., Brockhoff, P.B., and Christensen, R.H.B. (2017). lmerTest Package: Tests in Linear Mixed Effects Models. Journal of Statistical Software *82*, 1-26.

Lee, R., Chang, S.Y., Trinh, H., Tu, Y., White, A.C., Davies, B.S., Bergo, M.O., Fong, L.G., Lowry, W.E., and Young, S.G. (2010). Genetic studies on the functional relevance of the protein prenyltransferases in skin keratinocytes. Hum Mol Genet *19*, 1603-1617.

Leung, G.K., Schmidt, W.K., Bergo, M.O., Gavino, B., Wong, D.H., Tam, A., Ashby, M.N., Michaelis, S., and Young, S.G. (2001). Biochemical studies of Zmpste24-deficient mice. J Biol Chem *276*, 29051-29058.

Lin, F., and Worman, H.J. (1993). Structural organization of the human gene encoding nuclear lamin A and nuclear lamin C. J Biol Chem *268*, 16321-16326.

Lin, F., and Worman, H.J. (1995). Structural organization of the human gene (LMNB1) encoding nuclear lamin B1. Genomics *27*, 230-236.

Lopez-Mejia, I.C., Vautrot, V., De Toledo, M., Behm-Ansmant, I., Bourgeois, C.F., Navarro, C.L., Osorio, F.G., Freije, J.M., Stévenin, J., De Sandre-Giovannoli, A., Lopez-Otin, C., Lévy, N., Branlant, C., and Tazi, J. (2011). A conserved splicing mechanism of the LMNA gene controls premature aging. Hum Mol Genet *20*, 4540-4555.

Lutz, R.J., Trujillo, M.A., Denham, K.S., Wenger, L., and Sinensky, M. (1992). Nucleoplasmic localization of prelamin A: implications for prenylation-dependent lamin A assembly into the nuclear lamina. Proc Natl Acad Sci U S A *89*, 3000-3004.

Maeno, H., Sugimoto, K., and Nakajima, N. (1995). Genomic structure of the mouse gene (Lmnb1) encoding nuclear lamin B1. Genomics *30*, 342-346.

Marcos-Ramiro, B., Gil-Ordóñez, A., Marín-Ramos, N.I., Ortega-Nogales, F.J., Balabasquer, M., Gonzalo, P., Khiar-Fernández, N., Rolas, L., Barkaway, A., Nourshargh, S., Andrés, V., Martín-Fontecha, M., López-Rodríguez, M.L., and Ortega-Gutiérrez, S. (2021). Isoprenylcysteine Carboxylmethyltransferase-Based Therapy for Hutchinson-Gilford Progeria Syndrome. ACS Cent Sci *7*, 1300-1310.

Mirdita, M., Schütze, K., Moriwaki, Y., Heo, L., Ovchinnikov, S., and Steinegger, M. (2022). ColabFold: making protein folding accessible to all. Nat Methods *19*, 679-682.

Osorio, F.G., Navarro, C.L., Cadiñanos, J., López-Mejía, I.C., Quirós, P.M., Bartoli, C., Rivera, J., Tazi, J., Guzmán, G., Varela, I., Depetris, D., de Carlos, F., Cobo, J., Andrés, V., De Sandre-Giovannoli, A., Freije, J.M., Lévy, N., and López-Otín, C. (2011). Splicing-directed therapy in a new mouse model of human accelerated aging. Sci Transl Med *3*, 106ra107.

Paine, P.L., Moore, L.C., and Horowitz, S.B. (1975). Nuclear envelope permeability. Nature *254*, 109-114.

Park, H., Han, S.S., Sako, Y., and Pack, C.G. (2015). Dynamic and unique nucleolar microenvironment revealed by fluorescence correlation spectroscopy. FASEB J *29*, 837-848.

Quigley, A., Dong, Y.Y., Pike, A.C., Dong, L., Shrestha, L., Berridge, G., Stansfeld, P.J., Sansom, M.S., Edwards, A.M., Bountra, C., von Delft, F., Bullock, A.N., Burgess-Brown, N.A., and Carpenter, E.P. (2013). The structural basis of ZMPSTE24-dependent laminopathies. Science *339*, 1604-1607.

Raab, M., Gentili, M., de Belly, H., Thiam, H.R., Vargas, P., Jimenez, A.J., Lautenschlaeger, F., Voituriez, R., Lennon-Duménil, A.M., Manel, N., and Piel, M. (2016). ESCRT III repairs nuclear envelope ruptures during cell migration to limit DNA damage and cell death. Science *352*, 359-362.

Robijns, J., Molenberghs, F., Sieprath, T., Corne, T.D.J., Verschuuren, M., and De Vos, W.H. (2016). In silico synchronization reveals regulators of nuclear ruptures in lamin A/C deficient model cells. Sci Rep *6*, 30325.

Roblek, M., Schüchner, S., Huber, V., Ollram, K., Vlcek-Vesely, S., Foisner, R., Wehnert, M., and Ogris, E. (2010). Monoclonal antibodies specific for disease-associated point-mutants: lamin A/C R453W and R482W. PLoS One *5*, e10604.

Samson, C., Petitalot, A., Celli, F., Herrada, I., Ropars, V., Le Du, M.H., Nhiri, N., Jacquet, E., Arteni, A.A., Buendia, B., and Zinn-Justin, S. (2018). Structural analysis of the ternary complex between lamin A/C, BAF and emerin identifies an interface disrupted in autosomal recessive progeroid diseases. Nucleic Acids Res *46*, 10460-10473.

Sánchez-López, A., Espinós-Estévez, C., González-Gómez, C., Gonzalo, P., Andrés-Manzano, M.J., Fanjul, V., Riquelme-Borja, R., Hamczyk, M.R., Macías, A., Del Campo, L., Camafeita, E., Vázquez, J., Barkaway, A., Rolas, L., Nourshargh, S., Dorado, B., Benedicto, I., and Andrés, V. (2021). Cardiovascular Progerin Suppression and Lamin A Restoration Rescue Hutchinson-Gilford Progeria Syndrome. Circulation *144*, 1777-1794.

Santiago-Fernández, O., Osorio, F.G., Quesada, V., Rodríguez, F., Basso, S., Maeso, D., Rolas, L., Barkaway, A., Nourshargh, S., Folgueras, A.R., Freije, J.M.P., and López-Otín, C. (2019). Development of a CRISPR/Cas9-based therapy for Hutchinson-Gilford progeria syndrome. Nat Med *25*, 423-426.

Scaffidi, P., and Misteli, T. (2005). Reversal of the cellular phenotype in the premature aging disease Hutchinson-Gilford progeria syndrome. Nat Med *11*, 440-445.

Schibler, A.C., Jevtic, P., Pegoraro, G., Levy, D.L., and Misteli, T. (2023). Identification of epigenetic modulators as determinants of nuclear size and shape. Elife *12*, 10.1101/2022.1105.1128.493845.

Shimi, T., Butin-Israeli, V., Adam, S.A., Hamanaka, R.B., Goldman, A.E., Lucas, C.A., Shumaker, D.K., Kosak, S.T., Chandel, N.S., and Goldman, R.D. (2011). The role of nuclear lamin B1 in cell proliferation and senescence. Genes Dev *25*, 2579-2593.

Shimi, T., Kittisopikul, M., Tran, J., Goldman, A.E., Adam, S.A., Zheng, Y., Jaqaman, K., and Goldman, R.D. (2015). Structural organization of nuclear lamins A, C, B1, and B2 revealed by superresolution microscopy. Mol Biol Cell *26*, 4075-4086.

Shimi, T., Pack, C.G., and Goldman, R.D. (2016). Analyses of the Dynamic Properties of Nuclear Lamins by Fluorescence Recovery After Photobleaching (FRAP) and Fluorescence Correlation Spectroscopy

(FCS). Methods Mol Biol *1411*, 99-111.

Shimi, T., Pfleghaar, K., Kojima, S., Pack, C.G., Solovei, I., Goldman, A.E., Adam, S.A., Shumaker, D.K., Kinjo, M., Cremer, T., and Goldman, R.D. (2008). The A- and B-type nuclear lamin networks: microdomains involved in chromatin organization and transcription. Genes Dev *22*, 3409-3421.

Sinensky, M., Fantle, K., Trujillo, M., McLain, T., Kupfer, A., and Dalton, M. (1994). The processing pathway of prelamin A. J Cell Sci *107 (Pt 1)*, 61-67.

Taniura, H., Glass, C., and Gerace, L. (1995). A chromatin binding site in the tail domain of nuclear lamins that interacts with core histones. J Cell Biol *131*, 33-44.

Turgay, Y., Eibauer, M., Goldman, A.E., Shimi, T., Khayat, M., Ben-Harush, K., Dubrovsky-Gaupp, A., Sapra, K.T., Goldman, R.D., and Medalia, O. (2017). The molecular architecture of lamins in somatic cells. Nature *543*, 261-264.

Vargas, J.D., Hatch, E.M., Anderson, D.J., and Hetzer, M.W. (2012). Transient nuclear envelope rupturing during interphase in human cancer cells. Nucleus *3*, 88-100.

Voeltz, G.K., Rolls, M.M., and Rapoport, T.A. (2002). Structural organization of the endoplasmic reticulum. EMBO Rep *3*, 944-950.

Winter-Vann, A.M., and Casey, P.J. (2005). Post-prenylation-processing enzymes as new targets in oncogenesis. Nat Rev Cancer *5*, 405-412.

Yao, H., Chen, X., Kashif, M., Wang, T., Ibrahim, M.X., Tüksammel, E., Revêchon, G., Eriksson, M., Wiel, C., and Bergo, M.O. (2020). Targeting RAS-converting enzyme 1 overcomes senescence and improves progeria-like phenotypes of ZMPSTE24 deficiency. Aging Cell *19*, e13200.

Yu, K.R., Lee, S., Jung, J.W., Hong, I.S., Kim, H.S., Seo, Y., Shin, T.H., and Kang, K.S. (2013). MicroRNA-141-3p plays a role in human mesenchymal stem cell aging by directly targeting ZMPSTE24. J Cell Sci *126*, 5422-5431.

Zullo, J.M., Demarco, I.A., Piqué-Regi, R., Gaffney, D.J., Epstein, C.B., Spooner, C.J., Luperchio, T.R., Bernstein, B.E., Pritchard, J.K., Reddy, K.L., and Singh, H. (2012). DNA sequence-dependent compartmentalization and silencing of chromatin at the nuclear lamina. Cell *149*, 1474-1487.

Zwerger, M., Roschitzki-Voser, H., Zbinden, R., Denais, C., Herrmann, H., Lammerding, J., Grütter, M.G., and Medalia, O. (2015). Altering lamina assembly reveals lamina-dependent and -independent functions for A-type lamins. J Cell Sci *128*, 3607-3620.

Abbreviations

BAF, barrier-to-autointegration factor; CBD, chromatin-binding domain; cGAS, cyclic GMP-AMP synthase; DARPin, designed ankyrin repeat protein; DCM, dilated cardiomyopathy; ESCRT-III, endosomal sorting complex required for transport-III; ER, endoplasmic reticulum; FAF, fluorescence auto-correlation function; FCS, fluorescence correlation spectroscopy; FTI, farnesyltransferase inhibitor; FPLD, familial partial lipodystrophy; HGPS, Hutchinson-Gilford Progeria syndrome; Ig-fold, immunoglobulin-like fold; INM, inner nuclear membrane; KD, knockdown; KO, knockout; LA, lamin A; LACS, LA-characteristic segment; LB1, lamin B1; LB2, lamin B2; LC, lamin C; LINC, linker of nucleoskeleton and cytoskeleton; MEF, mouse embryonic fibroblast; MD, muscular dystrophy; NE, nuclear envelope; NL, nuclear lamina; non-p-BAF, non-phosphorylated BAF; NP, nucleoplasmic pool; NPC, nuclear pore complex; ONM, outer nuclear membrane; p-BAF, phosphorylated BAF; PG, progerin; REML, restricted maximum likelihood; sfGFP, superfolder GFP; sfCherry, superfolder Cherry; shRNA, short hairpin RNA; STING, stimulator of interferon genes; WT, wild type.

Figure legends

Figure 1. **The localization kinetics of LA and PG at sites of NE rupture induced by laser microirradiation in WT and G609G/+ MEFs. (A)** Protein architecture of LA and PG. The coiled-coil central rod domain (gray), the NLS (yellow), the β-strand comprising the IG-fold (blue), and the CaaX motif box (orange) are shown. Anti-LA antibody (4A58) and anti-PG antibody (RaPG) recognize LA- and PG-specific region, respectively, and they do not cross-react with each other. Anti-pre-LA antibody (7G11) recognize the adjacent site to the second proteolytic cleavage site, so do not cross-react with PG. **(B)** AFM is used to induce forced NE rupture. **(C)** Time-lapse images of NLS-sfCherry expressed in WT and G609G/+ MEFs before and after NE rupture induced by AFM indentation. The fluorescence intensities are indicated with rainbow color. Bar: 10 μm. **(D)** The nuclear-to-cytoplasmic intensity (N/C) ratio of NLS-sfCherry was measured and normalized to the initial intensities, and plotted to monitor NE rupture (means ± SEM; n = 20 cells from two independent experiments; ***, $P < 0.001$ from WT by a mixed effect model). **(E)** A 405-nm laser is used to induce NE rupture at a precise location on the NL. 13 to 21 cells are irradiated within 10 min, then incubated for 30, 60 and 120 min followed by fixation with 4% PFA/0.1% Triton-X 100. **(F** and **G)** A 2-μm diameter spot at the NE in cells was lase microirradiated to induce NE rupture, fixed at 30-130 min after incubation, and then stained with a combination of rabbit and mouse antibodies, followed by Alexa Fluor 488-labeled anti-rabbit and Cy5-labeled anti-mouse IgG, and Hoechst 33342 for DNA. Two independent experiments were performed. **(F)** Representative images of single confocal sections of WT and G609G/+ cells fixed within 60-70 min after laser microirradiation. Magnified views of the indicated areas by orange boxes are shown (bottom). The ruptured sites are indicated with yellow arrowheads (bottom). Bars: 5 μm (top) and 2μm (bottom). **(G)** Ratios of cells with (blue) and without (gray) localization of the indicated antibodies at NE rupture sites. The numbers of analyzed cells are indicated in the bar charts.

Figure 2. Repair of NE rupture and **rapid accumulation of LC at the rupture sites in WT and G609G/+ MEFs. (A)** Protein architecture of LA, LC and PG with sfGFP-DARPin-LA6. The summary of their dynamics is indicated on the right (+, accumulated at the rupture site; -, not accumulated). The structural image of sfGFP-DARPin-LA6 was predicted by AlphaFold2 (Mirdita *et al.*, 2022) and edited by the PyMOL (Schrödinger). **(B** and **C)** The sfGFP-DARPin-LA6 intensity at the rupture sites were measured with 10 s intervals, and the relative intensities are plotted (means ± SEM; n = 20 cells from two independent experiments). **(B)** Dynamics of the sfGFP-DARPin-LA6 in response to NE rupture in WT and G609G/+ cells. Magnified views of the indicated areas by orange boxes are shown (the second to fifth columns). A 2-μm diameter spot was laser-

microirradiated to induce NE rupture (yellow arrowheads). Bars: 5 μm (the first column) and 2 μm (the second to fifth columns). **(C)** Fluorescence intensities of sfGFP-DARPin-LA6 at the rupture sites were measured and normalized to the initial intensities. ***, P < 0.001 from WT by a mixed effect model). **(D** and **E)** The diffusion fraction of mEmerald-LC in WT and G609G/+ cells were measured by FCS. **(D)** A representative fluorescence image of mEmerald-LC before FCS measurements (top). The yellow crosses indicate the points measured by FCS. Bar, 10 μm. FCS measurements based on fluctuation analysis of fluorescence intensity. mEmerald-LC (Em-LC) move in or out of the confocal volume (white-out cylinder region in blue) at different speeds (bottom). **(E)** Diffusion coefficient of fast (Component 1; plotted in black) and slow component (Component 2; plotted in gray), mean ± SEM. Percentage of these components are indicated on the left to plots. ***, P < 0.001 compared to WT of Component 1 by a Welch's t-test.

Figure 3. **The localization kinetics at the rupture sites in FTI-treated WT and G609G/+ MEFs. (A)** Whole cell lysates from the indicated cells with 0.1% DMSO or 3.2 μM lonafarnib (FTI) were probed with anti-LA/C (3A6-4C11), anti-pre-LA (7G11), anti-mature-LA (4A4-A4), anti-PG, and anti-GAPDH (as loading control). Positions of the size standards are shown on the right. **(B)** Fluorescence intensities in the NP to the NL ratio of the anti-LA (4A58), anti-pre-LA (7G11) and anti-PG was measured after indirect immunofluorescence. ***, P < 0.001 compared to WT by a Welch's t-test. See Fig. S3 B for microscopic image. **(C)** Ratios of cells with (blue) and without (gray) localization of the indicated antibodies at NE rupture sites. The numbers of analyzed cells are indicated in the bar charts. **(D-F)** The diffusion fraction of mEmerald-LA (Em-LA) and mEmerald-PG (Em-PG) in WT and G609G/+ cells were measured by FCS. **(D)** Representative fluorescence fluctuations of each mEmerald-tagged lamins in the nucleoplasm plotted by count rate (green line for Em-LA and blue line for Em-PG) in WT (top) and G609G/+ cells (bottom). **(E** and **F)** Diffusion coefficient of fast (Component 1; plotted in black) and slow component (Component 2; plotted in gray) of Em-LA **(E)** and Em-PG **(F)** in indicated cells. Percentage of these components are indicated on the left to plots. N/A, not applicable because of pre-bleached. *, P < 0.05 from WT DMSO to G609G/+ DMSO of Component 1 by a Games–Howell test.

Figure 4. **The localization kinetics at the rupture sites in ZmpSte24-KD WT MEFs. (A)** Whole cell lysates from control (Scramble) and ZmpSte24-KD (shZmpste24) WT cells were probed with anti-pre-LA (7G11), anti-LA/C (3A6-4C11) and anti-GAPDH (as loading control). Positions of the size standards are shown on the right. **(B)** Scramble and shZmpste24 WT cells were indirect immunofluorescent stained with anti-LA (4A58) and anti-pre-LA (7G11). **(C)** Fluorescence intensities in the NP to the NL ratio of the anti-LA (4A58) and anti-pre-LA (7G11) were measured. **(D)** Representative images of single

confocal sections of Scramble and shZmpste24 WT cells fixed within 60-70 min after laser microirradiation. The ruptured sites with (blue arrowheads) or without (magenta arrowheads) localization of antibodies are indicated. Bar: 40 μm. **(E)** Ratios of cells with (blue) and without (gray) localization of the indicated antibodies at NE rupture sites. The numbers of analyzed cells are indicated in the bar charts.

Figure 5. **The localization kinetics at the rupture sites in FTI-treated ZmpSte24-KD WT MEFs. (A)** Whole cell lysates from the control (Scramble) and ZmpSte24-KD (shZmpste24) cells with 0.1% DMSO or 3.2 μM lonafarnib (FTI) were probed with anti-LA/C (3A6-4C11), anti-pre-LA (7G11), anti-mature-LA (4A4-A4), and anti-GAPDH (as loading control). Positions of the size standards are shown on the right. **(B)** Representative images of single confocal sections of Scramble and shZmpste24 WT cells with DMSO or FTI. Bar: 5 μm. **(C** and **D)** Fluorescence intensities in the NP to the NL ratio of the anti-pre-LA (7G11; **C**) and anti-mature-LA (4A4-A4; **D**) were measured. ***, $P < 0.001$ by a Games–Howell test. **(E)** Ratios of cells with (blue) and without (gray) localization of the indicated antibodies at NE rupture sites. The numbers of analyzed cells are indicated in the bar charts.

Figure 6. **The localization kinetics at the rupture sites in BAF-KD WT MEFs. (A)** Whole cell lysates from the control (Scramble) and BAF-KD (shBAF#1 and #2) cells were probed with anti-BANF1/BAF (EPR7668) and anti-GAPDH (as loading control). Positions of the size standards are shown on the right. **(B)** Representative images of single confocal sections of Scramble, shBAF#1 and #2 WT cells. Bar: 5 μm. **(C)** Fluorescence intensities in the NP to the NL ratio of the anti-LA (4A58) were measured. ***, $P < 0.001$ by a Games–Howell test. **(D)** Representative images of single confocal sections of Scramble, shBAF#1 and #2 WT cells fixed within 60-70 min after laser microirradiation. The ruptured sites with (blue arrowheads) or without (magenta arrowheads) localization of anti-LA are indicated. Bar: 40 μm. **(E)** Ratios of cells with (blue) and without (gray) localization of the indicated antibodies at NE rupture sites. The numbers of analyzed cells are indicated in the bar charts.

Figure 7. **Rapid accumulation of LA with C-terminal and internal deletion mutants at the rupture sites in LA/C-KO MEFs. (A)** Architecture of the deletion mutants of mEmerald-LA expressed from *Lmna* promoter vector. Terminal amino acids are numbered, and their accumulation dynamics is summarized on the right (+, accumulated at the rupture site; -, not accumulated). **(B)** Representative images of single confocal sections of mEmerald-LA-full-length (FL), L648X, T644X, F627X, S617X, A601X, S575X, and mEmerald-LC in LA/C-KO MEFs transfected for 2 d. Bar: 5 μm. **(C)** Fluorescence intensities in the NP to the NL ratio of mEmerald-LA mutants and

mEmerald-LC, as control, were measured. *, $P < 0.05$ and ‡, $P<0.001$ compared to all others by a Games–Howell test. **(D)** Fluorescence intensities of mEmerald-LA with C-terminal deletion mutants and mEmerald-LC, as control, at the rupture sites were measured and normalized to the initial intensities. ***, $P < 0.001$ from LA-FL by a mixed effect model). **(E)** Fluorescence intensities of mEmerald-LA with internal and C-terminal deletion mutants at the rupture sites were measured and normalized to the initial intensities. ***, $P < 0.001$ from LA-FL by a mixed effect model). LA-FL and LC are reproduction of D.

Figure 8. **Schematic diagram of fast accumulation and slow localization of A-type lamins. (A)** NE rupture and the rapid accumulation of LC (green) and later localization of LA (magenta) and PG (yellow) are depicted. Phosphorylated BAF (p-BAF) forms complexes with LA, PG and LC, and rapidly accumulates at NE rupture site. LA is slower to accumulate than LC because it contains two LACS in the tail (top). PG is difficult to accumulate because it has a farnesylated C-terminus (top). When cells are treated with FTI, PG accumulates as well as LA because it has non-farnesylated C-terminus, but they still accumulate slower than LC because of LACS (bottom).

Figure S1. **Phenotype characterization and the localization dynamics of LA and PG at the rupture sites in WT and G609G/+ MEFs. (A)** Phenotype characterization of WT and G609G/+ MEFs by immunofluorescence. Asterisk indicates cell with NE rupture due to the cell cycle and were excluded from the analysis. The misshapen, NE ruptured, mis-localized and cGAS accumulated nuclei are indicated with magenta arrowheads in DNA, NLS-sfCherry, anti-LB1 and anti-cGAS, respectively. **(B)** Representative images of single confocal sections of WT and G609G/+ cells fixed within 30-40 min (top) and 120-130 min (bottom) after laser microirradiation. Magnified views of the indicated areas by orange boxes are shown (bottom of each row). The ruptured sites are indicated with yellow arrowheads (bottom of each row). Bars: 5 μm (top of each row) and 2 μm (bottom of each row).

Figure S2. ***Rosa26* knock-in cells expressing A-type lamins under *Lmna* promoter for FCS analysis. (A)** The schematic diagram of linearized pLmna-Em-LA-R26Neo, pLmna-Em-PG-R26Neo and pLmna-Em-LC-R26Neo knock-in vectors. **(B)** Whole cell lysates from the indicated cells knocked-in with pLmna-Em-LA-R26Neo, pLmna-Em-PG-R26Neo and pLmna-Em-LC-R26Neo were probed with anti-LA/C (3A6-4C11) and anti-β-actin (as loading control). Positions of the size standards are shown on the right. **(C)** The diffusion fraction of Em-LC in WT and G609G/+ cells. ***, $P < 0.001$ from WT to G609G/+ by a Welch's t-test.

Figure S3. **The immunofluorescence, immunoblotting and diffusion fraction in FTI-treated WT and G609G/+ MEFs. (A)** Protein architecture of LA and PG with recognition regions of post-translational processing specific antibodies. Anti-mature-LA (4A4-A4) and anti-pre-LA (7G11) do not cross-react with each other and PG. **(B)** WT and G609G/+ MEFs treated with 0.1% DMSO (top) and 3.2 μM lonafarnib (FTI, bottom) were indirect immunofluorescent stained with anti-LA (4A58), anti-pre-LA (7G11) and anti-PG (RaPG). Bar: 5 μm. **(C)** Whole cell lysates from the indicated cells knocked-in with pLmna-Em-LA-R26Neo and pLmna-Em-PG-R26Neo treated with DMSO or FTI were probed with anti-LA/C (3A6-4C11) and anti-GAPDH (as loading control). Positions of the size standards are shown on the right. **(D)** The diffusion fraction of Em-LA and Em-PG in WT and G609G/+ cells. N/A, not applicable because of pre-bleached. **, $P < 0.01$, ***, $P < 0.001$ by a Games–Howell test.

Figure S4. **Accumulation dynamics of LA with C-terminal and internal deletion mutants at the rupture sites in LA/C-KO MEFs. (A)** Amino acid sequences of LA-(blue) or LC-specific (red) regions from *Homo sapiens* and *Mus musculus*. The amino acid homology is indicated as bars and a gap introduced between residue A600 and A601 to maximize homology. **(B)** Dynamics of the mEmerald-LA-S575X and A601X in

response to NE rupture in LA/C-KO MEFs. **(C)** Representative images of single confocal sections of mEmerald-LA-full-length (FL), LA-FL without LACS1 (LAΔ26), LAΔ26-L648X, LAΔ26-T644X, LAΔ26-F627X, and mEmerald-LC in LA/C-KO cells transfected for 2 d. Bar: 5 μm. **(D)** Fluorescence intensities in the NP to the NL ratio of mEmerald-LA mutants and mEmerald-LC, as control, were measured. ***, $P < 0.001$ by a Steel–Dwass test. **(E)** Dynamics of the mEmerald-LAΔ26-T644X and LAΔ26-F627X in response to NE rupture in LA/C-KO cells. **(B** and **E)** Magnified views of the indicated areas by orange boxes are shown (the second to fifth columns). A 2-μm diameter spot was laser-microirradiated to induce NE rupture (yellow arrowheads). Bars: 5 μm (the first column) and 2 μm (the second to fifth columns).

Fig. 1

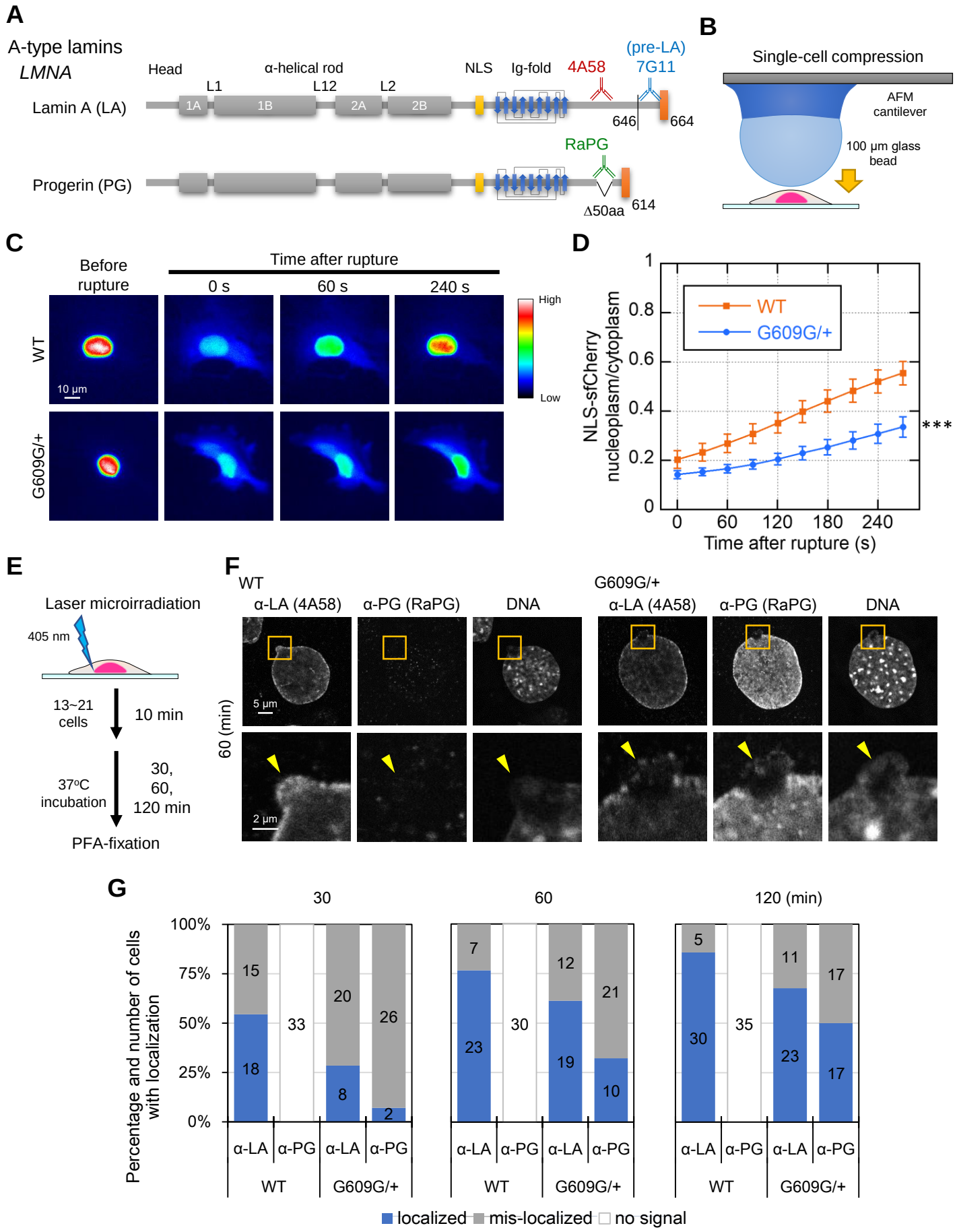
A
A-type lamins
LMNA
Head
α-helical rod
L1
L12
L2
NLS
Ig-fold
4A58
(pre-LA)
7G11
Lamin A (LA)
1A
1B
2A
2B
646
664
RaPG
Progerin (PG)
Δ50aa
614
B
Single-cell compression
AFM cantilever
100 μm glass bead
C
Before rupture
Time after rupture
0 s
60 s
240 s
WT
G609G/+
10 μm
High
Low
D
WT
G609G/+
NLS-sfCherry nucleoplasm/cytoplasm
Time after rupture (s)
***
E
Laser microirradiation
405 nm
13~21 cells
10 min
37°C incubation
30, 60, 120 min
PFA-fixation
F
WT
G609G/+
α-LA (4A58)
α-PG (RaPG)
DNA
60 (min)
5 μm
2 μm
G
30
60
120 (min)
Percentage and number of cells with localization
100%
75%
50%
25%
0%
α-LA
α-PG
WT
G609G/+
localized
mis-localized
no signal

Fig. 2

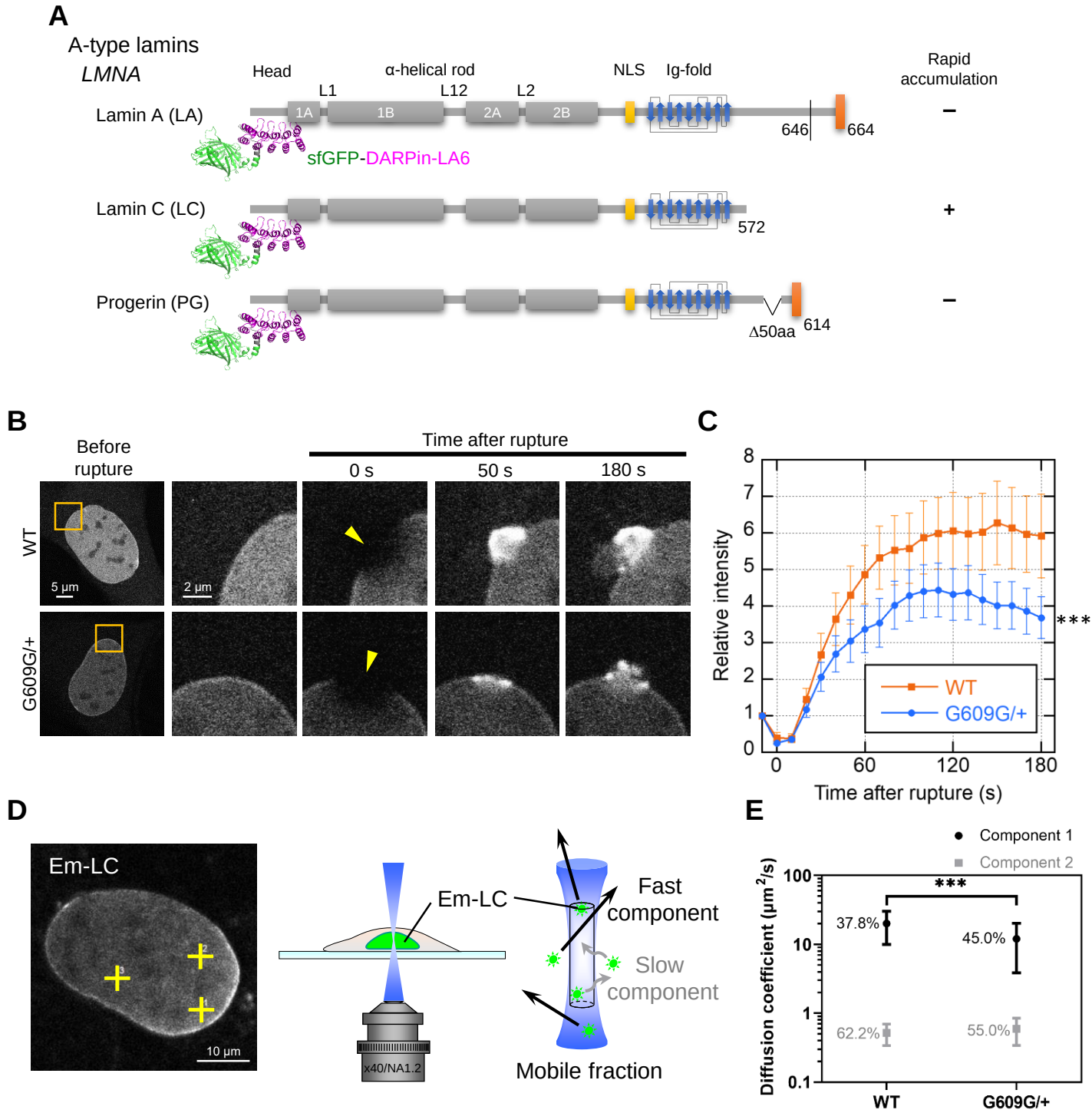
A
A-type lamins
LMNA
Head
α-helical rod
NLS
Ig-fold
Rapid accumulation
L1
L12
L2
1A
1B
2A
2B
Lamin A (LA)
646
664
–
sfGFP-DARPin-LA6
Lamin C (LC)
572
+
Progerin (PG)
Δ50aa
614
–
B
Before rupture
Time after rupture
0 s
50 s
180 s
WT
G609G/+
5 µm
2 µm
C
Relative intensity
Time after rupture (s)
WT
G609G/+
***
D
Em-LC
10 µm
Em-LC
Fast component
Slow component
Mobile fraction
x40/NA1.2
E
Component 1
Component 2
Diffusion coefficient (µm²/s)
***
37.8%
45.0%
62.2%
55.0%
WT
G609G/+

Fig. 3

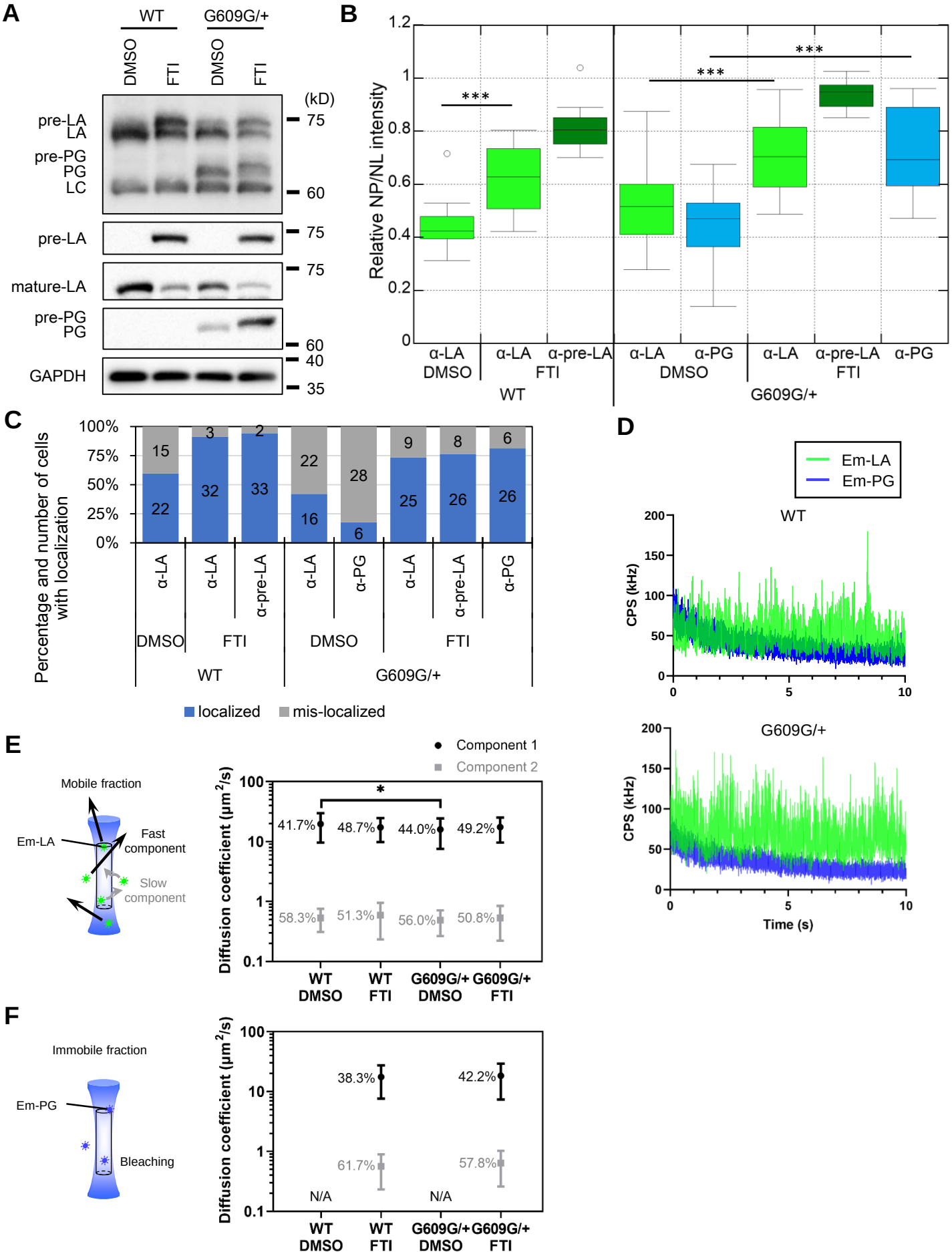
A
WT
G609G/+
DMSO
FTI
DMSO
FTI
(kD)
pre-LA
LA
pre-PG
PG
LC
75
60
pre-LA
75
mature-LA
75
pre-PG
PG
60
40
GAPDH
35
B
Relative NP/NL intensity
1.2
1
0.8
0.6
0.4
0.2
0
***
***
***
α-LA
α-LA
α-pre-LA
α-LA
α-PG
α-LA
α-pre-LA
α-PG
DMSO
FTI
DMSO
FTI
WT
G609G/+
C
Percentage and number of cells with localization
100%
75%
50%
25%
0%
15
22
3
32
2
33
22
16
28
6
9
25
8
26
6
26
α-LA
α-LA
α-pre-LA
α-LA
α-PG
α-LA
α-pre-LA
α-PG
DMSO
FTI
DMSO
FTI
WT
G609G/+
localized
mis-localized
D
Em-LA
Em-PG
WT
CPS (kHz)
200
150
100
50
0
0
5
10
G609G/+
CPS (kHz)
200
150
100
50
0
0
5
10
Time (s)
E
Mobile fraction
Em-LA
Fast component
Slow component
Component 1
Component 2
Diffusion coefficient (μm²/s)
100
10
1
0.1
*
41.7%
48.7%
44.0%
49.2%
58.3%
51.3%
56.0%
50.8%
WT DMSO
WT FTI
G609G/+ DMSO
G609G/+ FTI
F
Immobile fraction
Em-PG
Bleaching
Diffusion coefficient (μm²/s)
100
10
1
0.1
38.3%
42.2%
61.7%
57.8%
N/A
N/A
WT DMSO
WT FTI
G609G/+ DMSO
G609G/+ FTI

Fig. 4

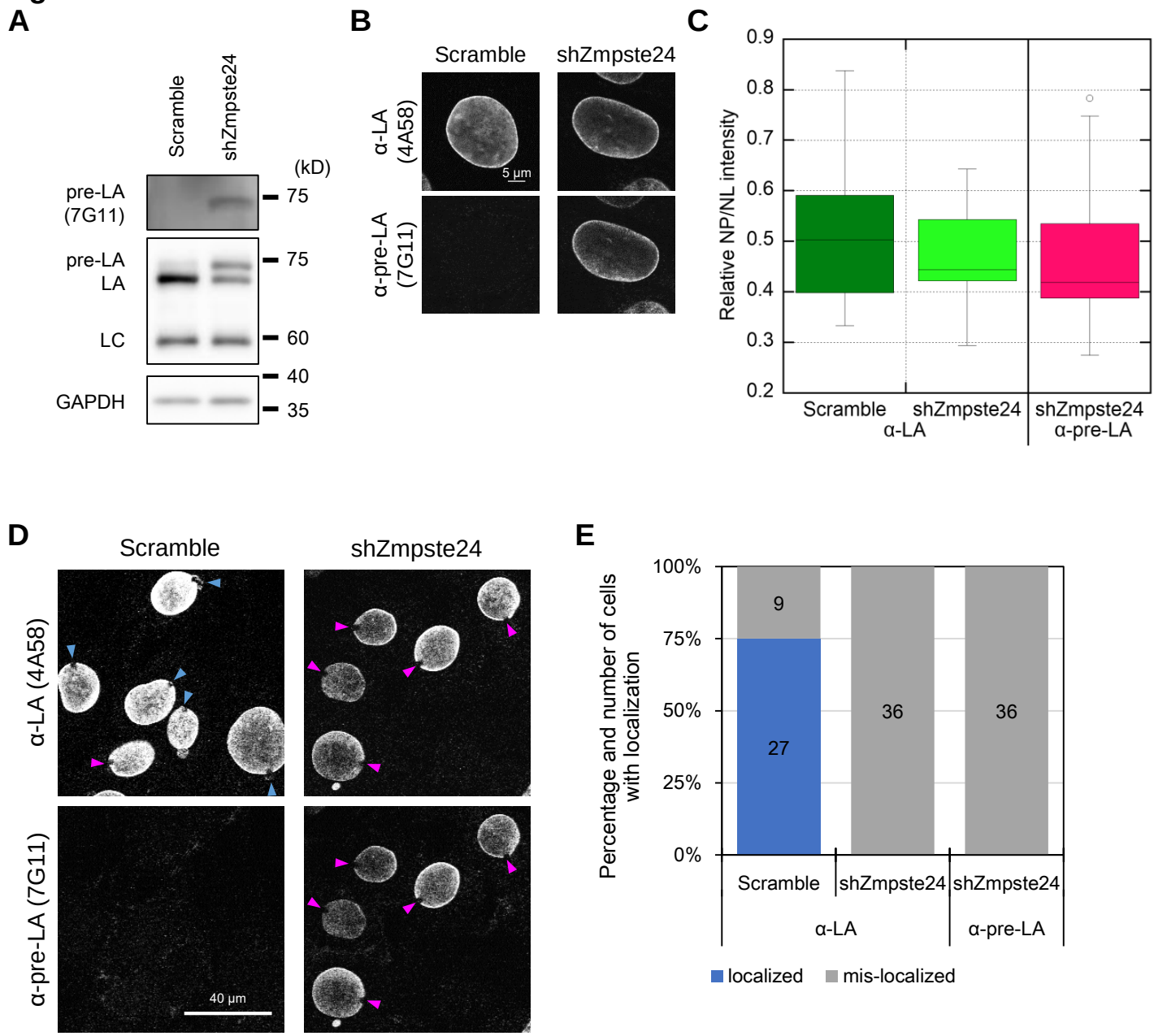
A
Scramble
shZmpste24
(kD)
pre-LA
(7G11)
75
pre-LA
LA
75
LC
60
40
GAPDH
35
B
Scramble
shZmpste24
α-LA
(4A58)
5 μm
α-pre-LA
(7G11)
C
Relative NP/NL intensity
0.9
0.8
0.7
0.6
0.5
0.4
0.3
0.2
Scramble
shZmpste24
α-LA
shZmpste24
α-pre-LA
D
Scramble
shZmpste24
α-LA (4A58)
α-pre-LA (7G11)
40 μm
E
Percentage and number of cells with localization
100%
75%
50%
25%
0%
9
27
36
36
Scramble
shZmpste24
shZmpste24
α-LA
α-pre-LA
localized
mis-localized

Fig. 5

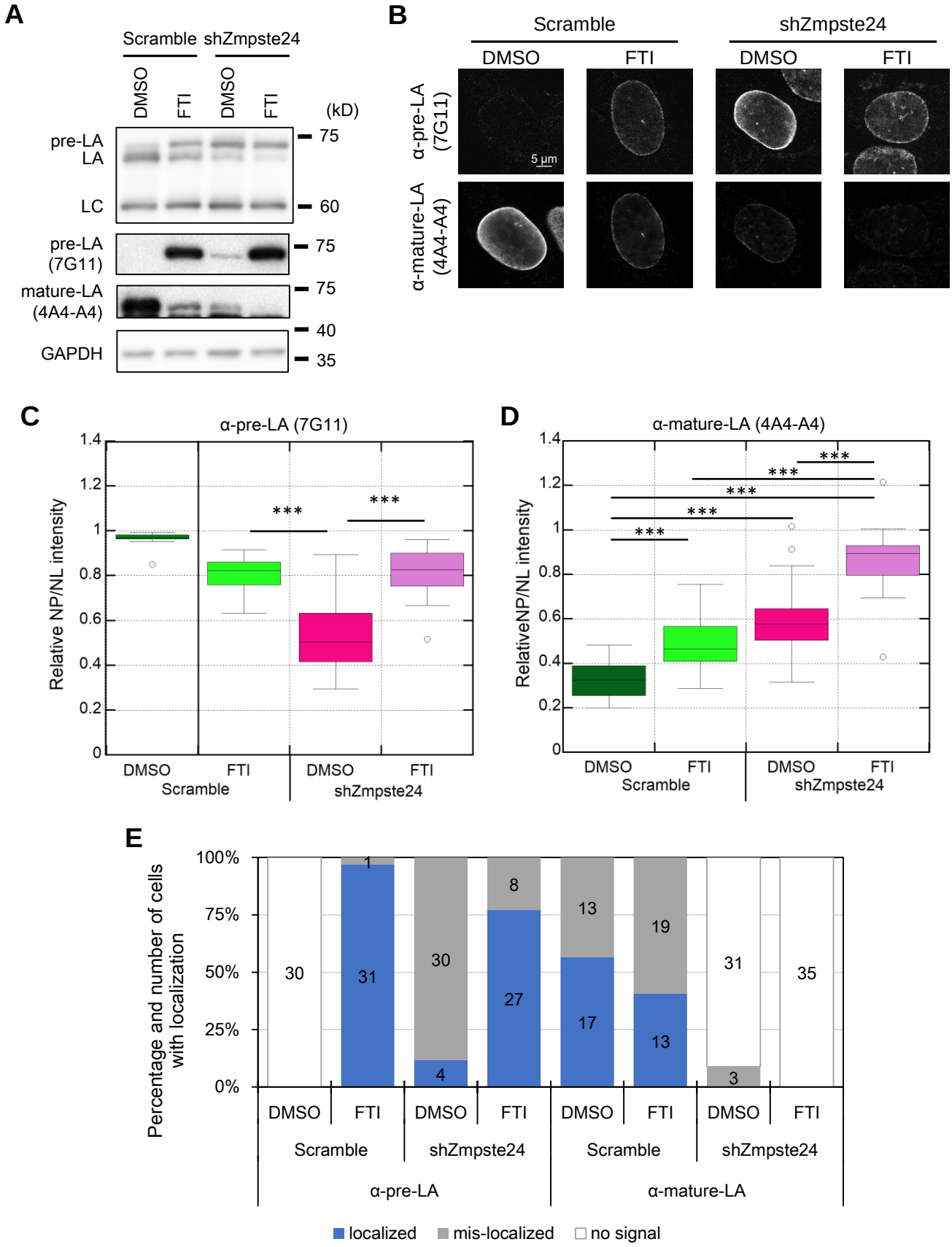
A
Scramble
shZmpste24
DMSO
FTI
DMSO
FTI
(kD)
pre-LA
LA
LC
pre-LA
(7G11)
mature-LA
(4A4-A4)
GAPDH
75
60
75
75
40
35
B
Scramble
shZmpste24
DMSO
FTI
DMSO
FTI
α-pre-LA
(7G11)
α-mature-LA
(4A4-A4)
5 μm
C
α-pre-LA (7G11)
Relative NP/NL intensity
1.4
1.2
1
0.8
0.6
0.4
0.2
0
***
***
DMSO
FTI
DMSO
FTI
Scramble
shZmpste24
D
α-mature-LA (4A4-A4)
RelativeNP/NL intensity
1.4
1.2
1
0.8
0.6
0.4
0.2
0
***
***
***
***
***
DMSO
FTI
DMSO
FTI
Scramble
shZmpste24
E
Percentage and number of cells
with localization
100%
75%
50%
25%
0%
30
1
31
30
4
8
27
13
17
19
13
31
3
35
DMSO
FTI
DMSO
FTI
DMSO
FTI
DMSO
FTI
Scramble
shZmpste24
Scramble
shZmpste24
α-pre-LA
α-mature-LA
localized
mis-localized
no signal

Fig. 6

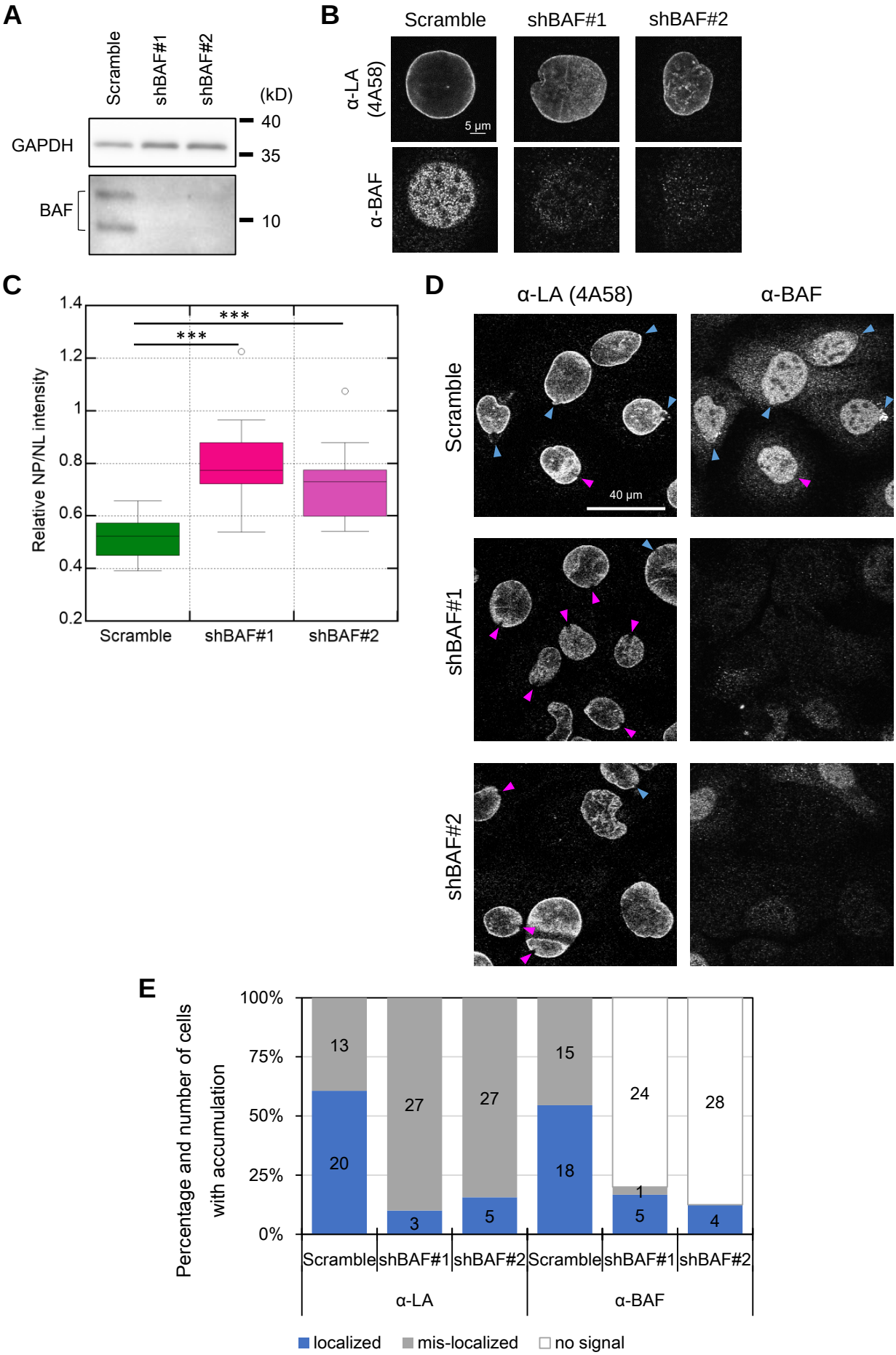
A
Scramble
shBAF#1
shBAF#2
(kD)
GAPDH
BAF
40
35
10
B
Scramble
shBAF#1
shBAF#2
α-LA (4A58)
α-BAF
5 μm
C
Relative NP/NL intensity
1.4
1.2
1
0.8
0.6
0.4
0.2
***
***
Scramble
shBAF#1
shBAF#2
D
α-LA (4A58)
α-BAF
Scramble
shBAF#1
shBAF#2
40 μm
E
Percentage and number of cells with accumulation
100%
75%
50%
25%
0%
13
20
27
3
27
5
15
18
24
1
5
28
4
Scramble
shBAF#1
shBAF#2
Scramble
shBAF#1
shBAF#2
α-LA
α-BAF
localized
mis-localized
no signal

Fig. 7

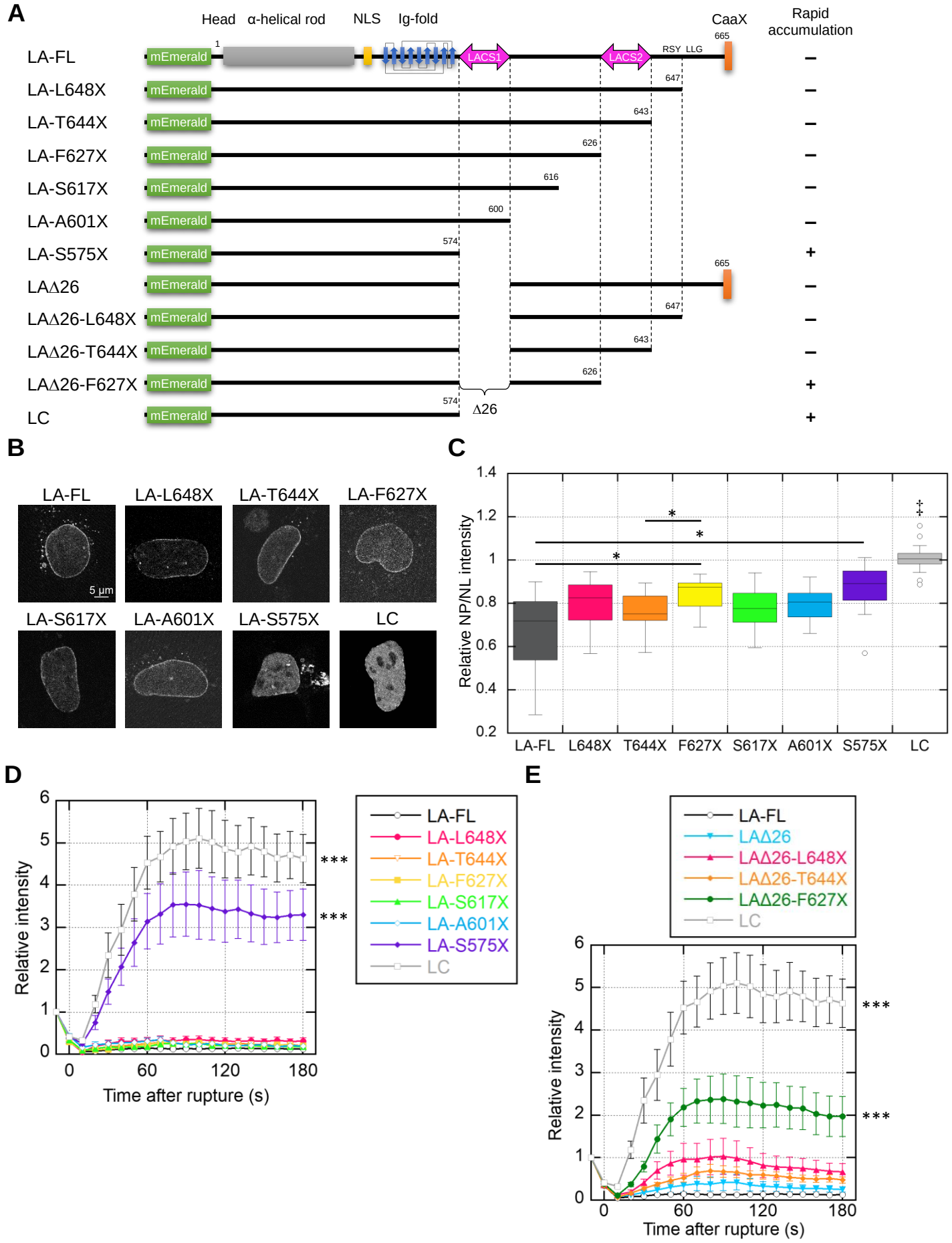
A
Head
α-helical rod
NLS
Ig-fold
CaaX
Rapid accumulation
LA-FL
LA-L648X
LA-T644X
LA-F627X
LA-S617X
LA-A601X
LA-S575X
LAΔ26
LAΔ26-L648X
LAΔ26-T644X
LAΔ26-F627X
LC
mEmerald
LACS1
LACS2
RSY LLG
Δ26
B
5 μm
C
Relative NP/NL intensity
D
Relative intensity
Time after rupture (s)
E
LAΔ26
LAΔ26-L648X
LAΔ26-T644X
LAΔ26-F627X

Fig. 8

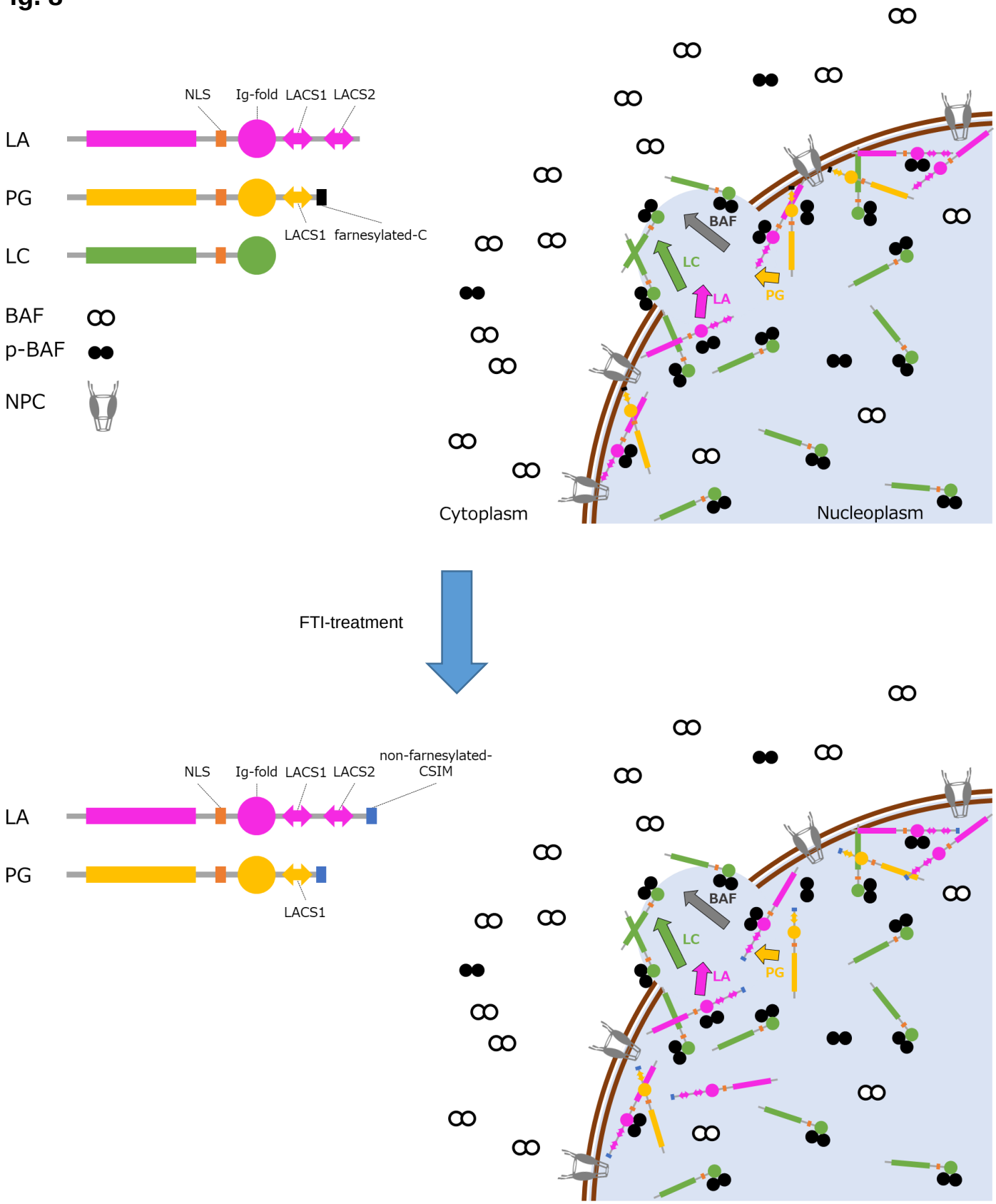
NLS
Ig-fold
LACS1
LACS2
LA
PG
LACS1
farnesylated-C
LC
BAF
p-BAF
NPC
BAF
LC
LA
PG
Cytoplasm
Nucleoplasm
FTI-treatment
non-farnesylated-CSIM
NLS
Ig-fold
LACS1
LACS2
LA
PG
LACS1
BAF
LC
LA
PG

Table S1. Phenotype characterization of WT and G609G/+ MEFs

	WT (n = 118 cells, 129 nuclei)	G609G/+ (n = 116 cells, 131 nuclei)	P value
DNA			0.465
normal	122 (94.6%)	120 (91.6%)	
mis-shapen	7 (5.4%)	11 (8.4%)	
NLS-sfCherry			0.102
nuclear-localized	110 (93.2%)	114 (98.3%)	
ruptured	8 (6.8%)	2 (1.7%)	
α-LB1			0.212
normal distributed	125 (96.9%)	130 (99.2%)	
mis-localized	4 (3.1%)	1 (0.8%)	
α-cGAS			1
not accumulated	129 (100%)	131 (100%)	
accumulated	0 (0%)	0 (0%)	

Table S2. Oligonucleotides used in this study

No.	Name	Sequence (5' to 3')
1	shSte24#1-TRCN0000366641_S	CCGGCTGGATGCTCTTCCGGTTATTCTCGAGAATAACCGGAAGAGCATCCAGTTTTTG
2	shSte24#1-TRCN0000366641_AS	AATTCAAAAACTGGATGCTCTTCCGGTTATTCTCGAGAATAACCGGAAGAGCATCCAG
3	shBanf1#1-TRCN0000124958_Fw	CCGGTGGCCAGTTTCTGGTGCTAAACTCGAGTTTAGCACCAGAAACTGGCCATTTTTG
4	shBanf1#1-TRCN0000124958_Rv	AATTCAAAAATGGCCAGTTTCTGGTGCTAAACTCGAGTTTAGCACCAGAAACTGGCCA
5	shBanf1#2-TRCN0000124955_Fw	CCGGGACAAGGCTTATGTGGTCCTTCTCGAGAAGGACCACATAAGCCTTGTCTTTTTG
6	shBanf1#2-TRCN0000124955_Rv	AATTCAAAAAGACAAGGCTTATGTGGTCCTTCTCGAGAAGGACCACATAAGCCTTGTC
7	pX459V2-Fw	GAATTCTAACTAGAGCTCGCTGATCAGCCTCG
8	pX459V2-Rv	TGGGCCAGGATTCTCCTCGACGTCAC
9	if_mCherry_Fw	GAGAATCCTGGCCCAATGGTGAGCAAGGGCGAGGAGG
10	if_mCherry_Rv	CTCTAGTTAGAATTCTCACTTGTACAGCTCGTCCATGCCGCCGG
11	sgRosa26-1_s	CACCGACTCCAGTCTTTCTAGAAGA
12	sgRosa26-1_as	AAACTCTTCTAGAAAGACTGGAGTC
13	if_LA promoter_Fw	ATGCATTAGTTATTAATTGCCTCGAAAAACCAAAAAAAG
14	if_LA promoter_Rv	GACCGGTAGCGCTAGCCCGCTGTGACGGGGTCTCCATG
15	if_mLA_Fw	ATGGAGACCCCGTCACAGCGG
16	if_mLA_Rv	AACCGGTAGCGCTAGCCATGATGCTGCAGTTCTGGG
17	mLA-to-PG_Fw	CAGAGCTCCCAGAACTGCAGC
18	mLA-to-PG_Rv	TCTGGGAGCTCTGGGCTCCCGCTCCACCG
19	mLA-L648X_Fw (mature)	CACCCGCTCCTACTAGCTGGGCAACTCC
20	mLA-L648X_Rv (mature)	GGAGTTGCCCAGCTAGTAGGAGCGGGTG
21	mLA-T644X_Fw	GACAACCTAGTCTAACGCTCCTACCTC
22	mLA-T644X_Rv	GAGGTAGGAGCGTTAGACTAGGTTGTC
23	mLA-F627X_Fw	GTCACTCGAAGCTGACGCAGTGTGGGG
24	mLA-F627X_Rv	CCCCACACTGCGTCAGCTTCGAGTGAC
25	mLA-S617X_Fw	CCTCTGGCTCTTGAGCCTCCAGTGTC
26	mLA-S617X_Rv	GACACTGGAGGCTCAAGAGCCAGAGG
27	mLA-A601X_Fw	GCTGACAAGGCTTGAGGTGGAGCGGGAG
28	mLA-A601X_R2	CTCCCGCTCCACCTCAAGCCTTGTCAGCAG
29	mLA-S575X_Fw	CACTGCAGCGGCTAGGGGGACCCCGC
30	mLA-S575X_Rv	GCGGGGTCCCCCTAGCCGCTGCAGTG
31	if_mLA-del575-600_Fw	CAGCGGCGCCGGTGGAGCGGGAGCCC
32	if_mLA-del575-600_Rv	CCACCGGCGCCGCTGCAGTGGGAACCAC
33	if_Rosa26L-mLA_Fw	GTCTTTCTAGCCTTAATTAATGCCTCGAAAAACCAAAA
34	if_mLA-bGHpA-Rv	GAGGTCGACCAATTGTTACATGATGCTGCAGTTCTG
35	if_bGHpA_Fw	CAATTGGTCGACCTCGACCTCGACTG
36	if_Rosa26R-bGHpA_Rv	GCGGCCGCCGCGCCCACGCGTTCCCCAGCATGCC
37	if_Nsi-BGHpA_Fw	GGCAGCCGCCGCTGAATGCATCAATTGGTCGACCTCGACCTCGACTGT
38	if_mLA-to-mLC_Rv	TCAGCGGCGGCTGCCACTCACACGGTGGTGATGGAGGAGCTCTTCT

See Materials and methods. Oligonucleotides were synthesized by Integrated DNA Technologies (IDT) or Sigma-Aldrich.

Fig. S1

A

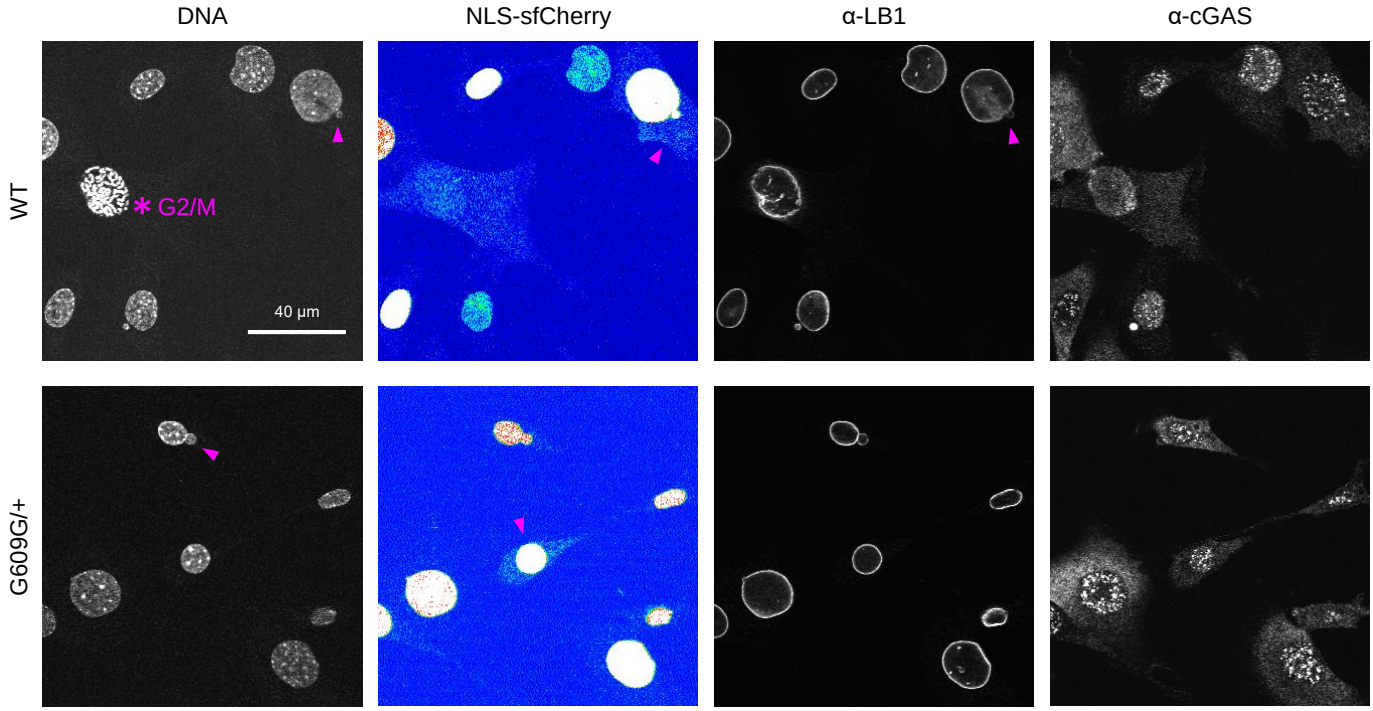
DNA
NLS-sfCherry
α-LB1
α-cGAS
WT
G609G/+
* G2/M
40 µm

B

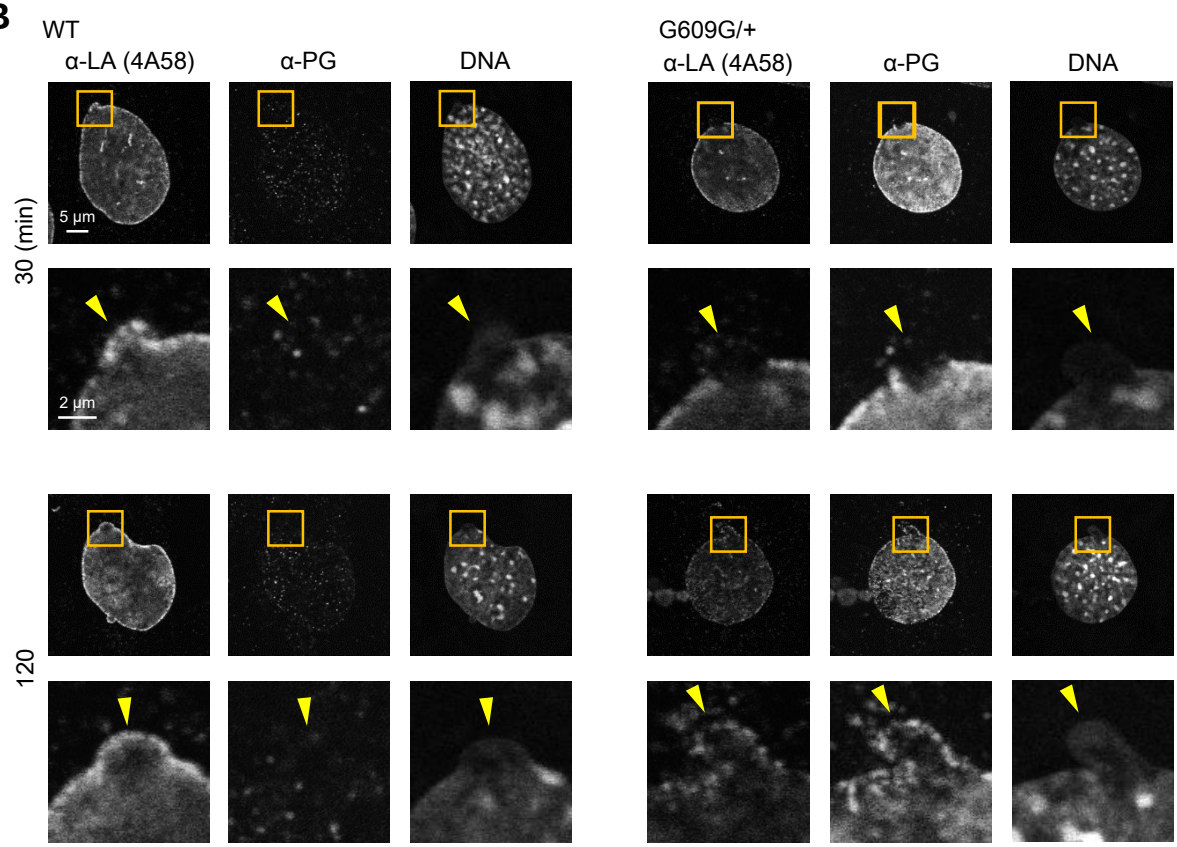
WT
G609G/+
α-LA (4A58)
α-PG
DNA
30 (min)
120
5 µm
2 µm

Fig. S2

A

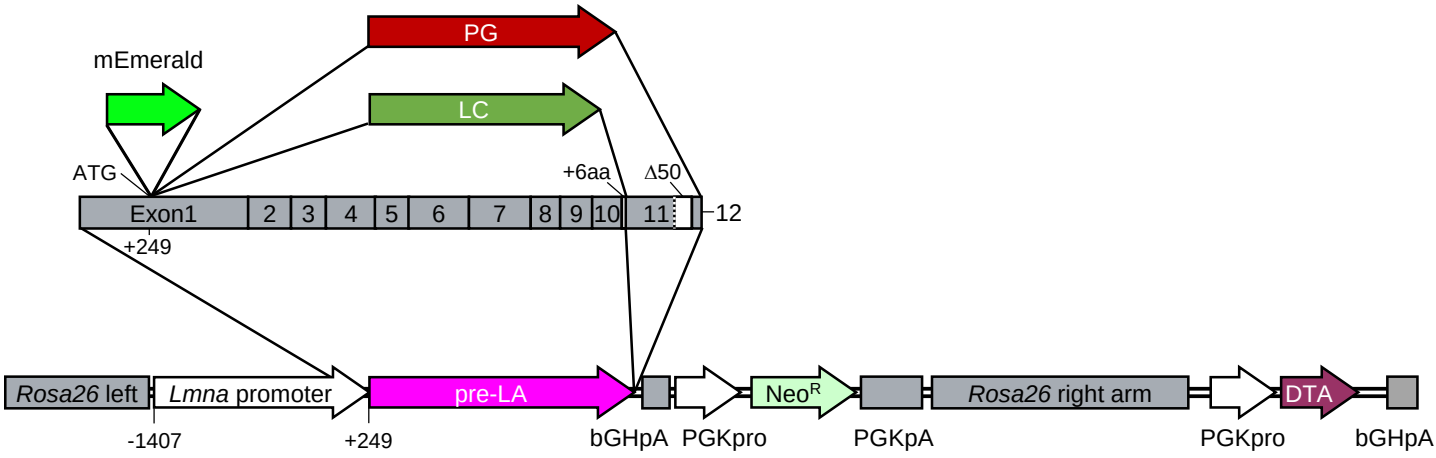
PG
mEmerald
LC
ATG
+6aa
Δ50
Exon1
2
3
4
5
6
7
8
9
10
11
12
+249
Rosa26 left
Lmna promoter
pre-LA
NeoR
Rosa26 right arm
DTA
-1407
+249
bGHpA
PGKpro
PGKpA
PGKpro
bGHpA

B

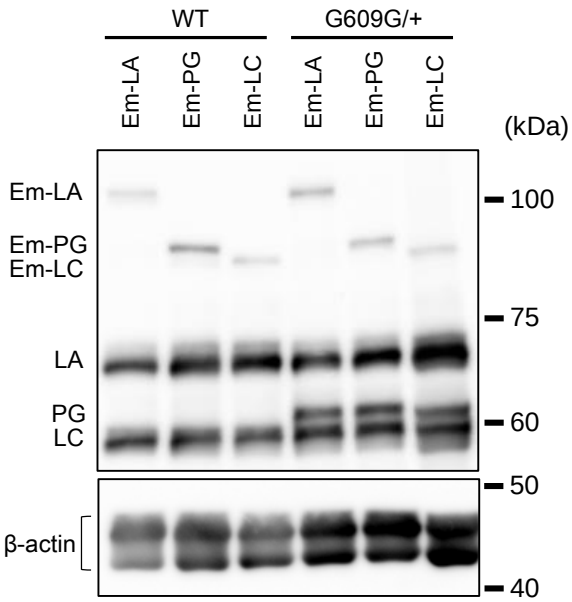
WT
G609G/+
Em-LA
Em-PG
Em-LC
Em-LA
Em-PG
Em-LC
(kDa)
Em-LA
Em-PG
Em-LC
LA
PG
LC
β-actin
100
75
60
50
40

Fig. S3

A

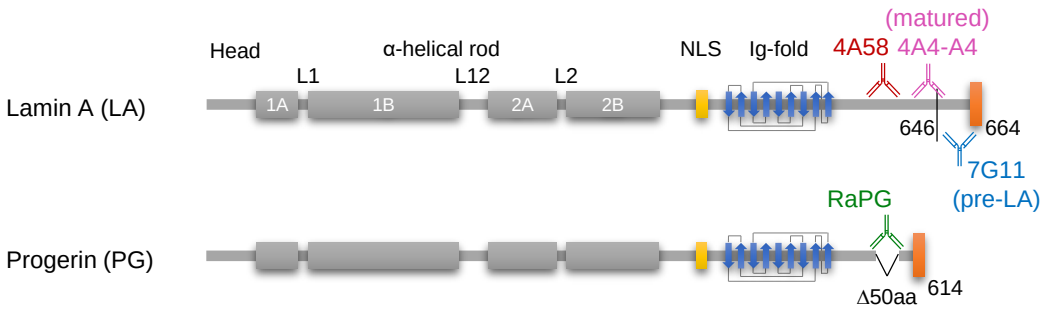
Head
α-helical rod
NLS
Ig-fold
(matured)
4A58
4A4-A4
L1
L12
L2
Lamin A (LA)
1A
1B
2A
2B
646
664
7G11
(pre-LA)
RaPG
Progerin (PG)
Δ50aa
614

B

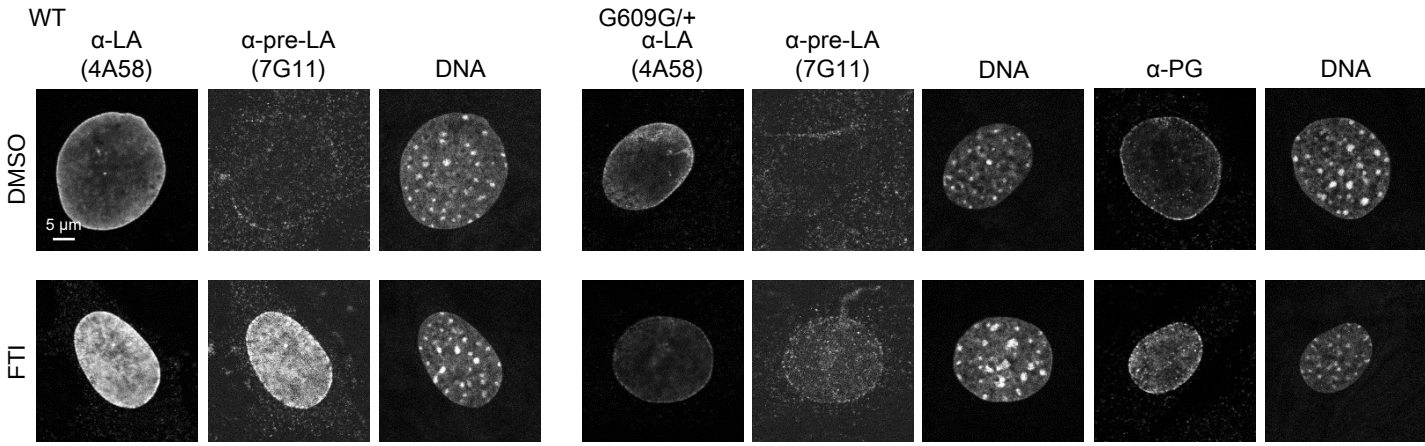
WT
α-LA
(4A58)
α-pre-LA
(7G11)
DNA
G609G/+
α-LA
(4A58)
α-pre-LA
(7G11)
DNA
α-PG
DNA
DMSO
FTI
5 μm

C

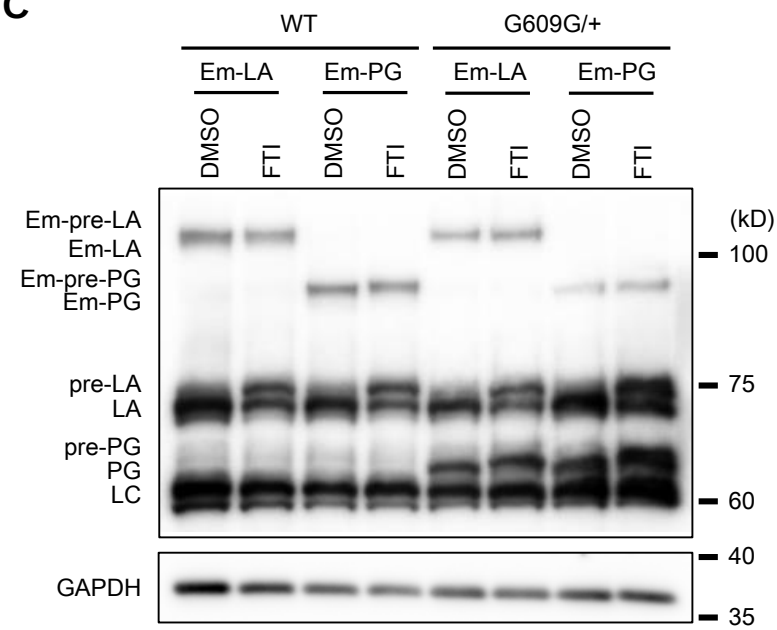
WT
G609G/+
Em-LA
Em-PG
Em-LA
Em-PG
DMSO
FTI
DMSO
FTI
DMSO
FTI
DMSO
FTI
Em-pre-LA
Em-LA
Em-pre-PG
Em-PG
pre-LA
LA
pre-PG
PG
LC
GAPDH
(kD)
100
75
60
40
35

Fig. S4

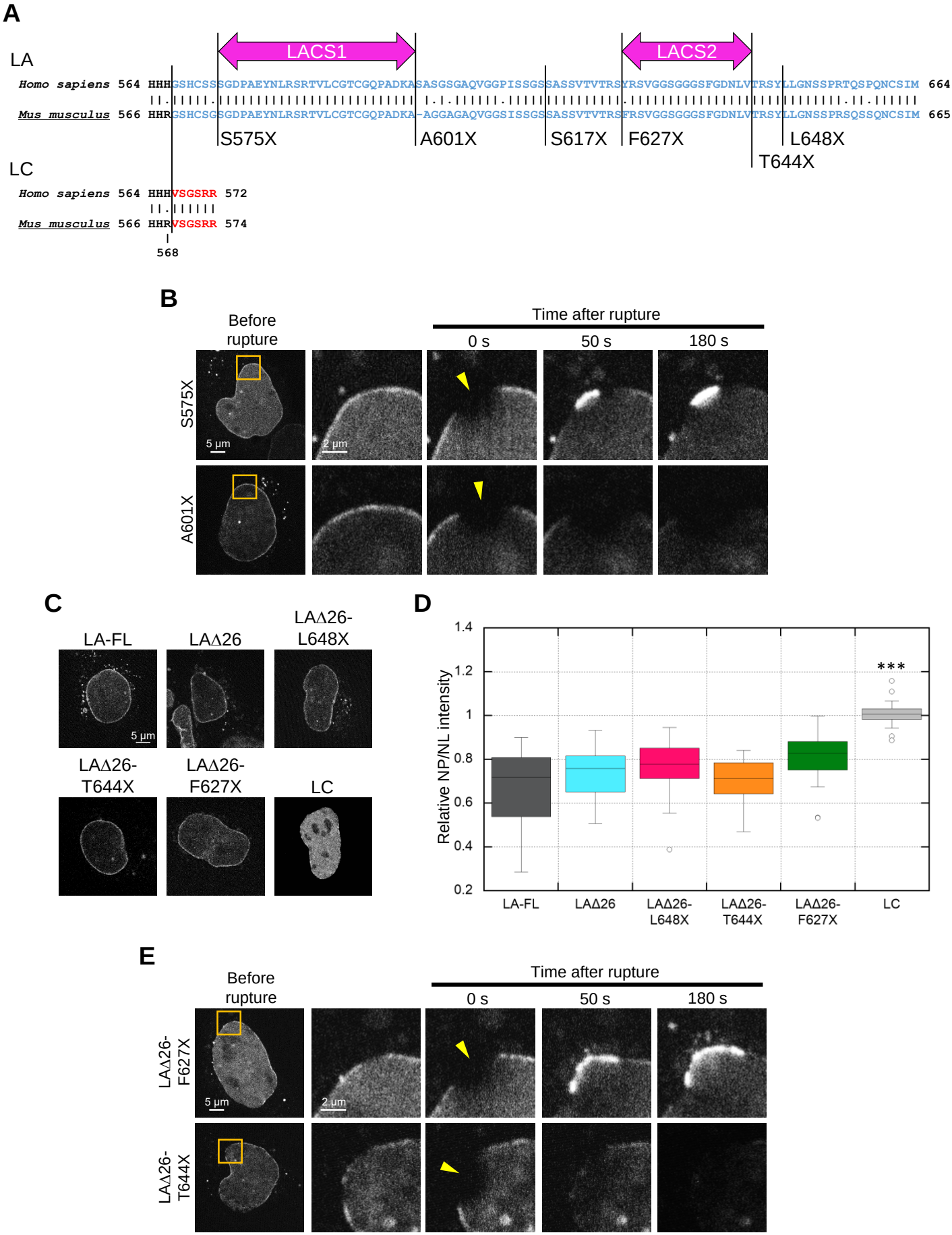
A
LA
LACS1
LACS2
Homo sapiens 564 HHHGSHCSSSGDPAEYNLRSRTVLCGTCGQPADKASASGSGAQVGGPISSGSSASSVTVTRSYRSVGGSGGGSFGDNLVTRSYLLGNSSPRTQSPQNCSIM 664
Mus musculus 566 HHRGSHCSGSGDPAEYNLRSRTVLCGTCGQPADKA-AGGAGAQVGGSISSGSSASSVTVTRSFRSVGGSGGGSFGDNLVTRSYLLGNSSPRSQSSQNCSIM 665
S575X
A601X
S617X
F627X
L648X
T644X
LC
Homo sapiens 564 HHHVSGSRR 572
Mus musculus 566 HHRVSGSRR 574
568
B
Before rupture
Time after rupture
0 s
50 s
180 s
S575X
A601X
5 µm
2 µm
C
LA-FL
LAΔ26
LAΔ26-L648X
LAΔ26-T644X
LAΔ26-F627X
LC
5 µm
D
Relative NP/NL intensity
1.4
1.2
1
0.8
0.6
0.4
0.2
***
LA-FL
LAΔ26
LAΔ26-L648X
LAΔ26-T644X
LAΔ26-F627X
LC
E
Before rupture
Time after rupture
0 s
50 s
180 s
LAΔ26-F627X
LAΔ26-T644X
5 µm
2 µm